Journal of Computational Physics 229 (2010) 3573–3604

Contents lists available at ScienceDirect

Journal of Computational Physics

journal homepage: www.elsevier.com/locate/jcp

HLLC-type Riemann solver for the Baer–Nunziato equations of compressible two-phase flow

S.A. Tokareva, E.F. Toro *

Laboratory of Applied Mathematics, Department of Civil and Environmental Engineering, University of Trento, Italy

ARTICLE INFO

Article history:
Received 5 October 2009
Received in revised form 9 January 2010
Accepted 15 January 2010
Available online 4 February 2010

Keywords:
Compressible multiphase flow
Hyperbolic equations
Nonconservative products
Complete Riemann solvers
HLLC solver
Finite volumes
DG finite elements
Path-conservative methods

ABSTRACT

We first construct an approximate Riemann solver of the HLLC-type for the Baer–Nunziato equations of compressible two-phase flow for the "subsonic" wave configuration. The solver is fully nonlinear. It is also complete, that is, it contains all the characteristic fields present in the exact solution of the Riemann problem. In particular, stationary contact waves are resolved exactly. We then implement and test a new upwind variant of the path-conservative approach; such schemes are suitable for solving numerically nonconservative systems. Finally, we use locally the new HLLC solver for the Baer–Nunziato equations in the framework of finite volume, discontinuous Galerkin finite element and path-conservative schemes. We systematically assess the solver on a series of carefully chosen test problems.

1. Introduction

The Baer–Nunziato equations are a first-order system of 11 nonlinear partial differential equations that model the dynamics of a three-dimensional flowing mixture of two compressible materials or phases, typically a solid particle phase and a gaseous phase. The model was first proposed by Baer and Nunziato [1] in the context of granular energetic combustible materials embedded in gaseous combustion products. Distinctive features of the Baer–Nunziato model are that it admits two velocity vectors and two pressures. Several mathematical models for multiphase flows have a similar form to that of the original Baer–Nunziato equations. See for example [2–6]. From a numerical point of view it is therefore justified to concentrate on the Baer–Nunziato equations, while still retaining a degree of generality. The mathematical character of the one-dimensional homogeneous (no source terms) equations was comprehensively studied by Embid and Baer [7]. The equations are hyperbolic, except for some well identified situations, and the complete mathematical structure of the 1D system is available. However, the equations cannot be written in conservation-law form, or divergence form. In other words, when the equations are written in terms of the conserved variables for each phase there are nonconservative products present and the classical Rankine–Hugoniot conditions to define shocks are not available. The nonconservative form of the equations has for a long time remained a challenge from both the mathematical and numerical points of view.

This paper is primarily concerned with the Riemann problem for the Baer–Nunziato equations. This is the simplest initial value problem worth studying. First, it gives insight into the behaviour of nonlinear wave propagation contained in the full system. Second, its solution furnishes a basic tool, a Riemann solver, for numerical methods for solving the general

* Corresponding author. Tel.: +39 0461 882674; fax: +39 0461 882676.
E-mail addresses: s_tokareva@mail.ru (S.A. Tokareva), toro@ing.unitn.it (E.F. Toro).

0021-9991/$ - see front matter © 2010 Elsevier Inc. All rights reserved.
doi:10.1016/j.jcp.2010.01.016

initial-boundary value problem. The first reported solution to the Riemann problem for the Baer–Nunziato equations is due to Andrianov and Warnecke [8]. Such solution is however *indirect*: they assume a solution and then look for initial data that corresponds to the assumed solution. In practice, especially for numerical purposes, one requires the *direct* solution, that is, given the piecewise constant initial conditions we want to find the corresponding solution at a later time. The first direct Riemann solver was reported by Schwendeman et al. [9]. See also the recent work of Deledicque and Papalexandris [6]. Riemann solvers are used to construct upwind numerical methods in the classical frameworks of finite volume and discontinuous Galerkin finite element methods. Riemann solvers can also be used in the frame of path-conservative methods [10], a recent class of schemes specially designed to approximate hyperbolic equations that contain nonconservative products. Perhaps the earliest reported attempt to incorporate the Riemann problem into a numerical scheme for compressible two-phase flow is that reported in [11], with encouraging results. More recent works in this direction include [12–17], to name but a few. Analysis and experience shows that upwind schemes are the most accurate schemes, provided however, they are based on *complete Riemann solvers*, that is, Riemann solvers that account for all the characteristic fields present in the exact solution of the Riemann problem. In other words, the wave model of the approximate Riemann solver contains the same number of waves as the exact Riemann solver. Devising complete Riemann solvers for large hyperbolic systems is, however, a difficult or impossible task, and it is here where centred, or non-upwind, methods have a clear advantage over upwind methods. There are several approaches for constructing approximate Riemann solvers, see [18], for example. Here we adopt the HLLC approach first reported in [19,20] for the Euler equations. See also [21,22] for further developments.

In this paper we extend the HLLC approach to the one-dimensional Baer–Nunziato equations in the normal direction to an arbitrary volume edge of a three-dimensional finite volume or element, resulting in a one-dimensional hyperbolic system of 11 equations in nonconservative form. To construct the solver, we first apply the HLLC approach based on integral averaged Rankine–Hugoniot relations across the nonlinear waves, for each phase. This is possible because away from the linearly degenerate solid contact wave the phases decouple and the equations recover their conservative character. This step connects the initial data on the left and right states to the unknown states behind the nonlinear waves. We then connect such states across the solid linearly degenerate field using jump conditions based on a thin-layer theory reported in [9]. The resulting jump conditions can also be obtained by simply applying generalized Riemann invariants, as in [7]. The final result is a nonlinear algebraic system of four equations connecting the unknowns to the initial conditions left and right of the interface. Surprisingly, only two iterations of the Newton method are sufficient to achieve an accurate solution of the Riemann problem and therefore the method becomes essentially a predictor–corrector method. The resulting HLLC-type approximate Riemann solver is fully nonlinear. The solver is also complete, as it contains all the characteristic fields present in the exact solution of the Riemann problem. This feature is most important for resolving intermediate waves, such as contact and shear waves, with minimal numerical dissipation. Our solver, when implemented in a shock-capturing method, resolves exactly isolated stationary contact discontinuities and shear waves. As a second contribution of this paper we implement and thoroughly test a new upwind path-conservative method, which opens the way to the use of different state Riemann solvers. Here we implement and test the new HLLC solver for the Baer–Nunziato equations. In addition, in order to illustrate the potential of the HLLC solver of this paper, we also implement it in the frame of finite volume and discontinuous Galerkin finite element schemes. We systematically assess the solver on a series of carefully chosen tests problems. The Riemann solver for the Baer–Nunziato equations based on the HLLC approach proves to be simpler and faster than the exact solver proposed in [9] and at the same time provides virtually the same solution quality.

The rest of this paper is organized as follows. In Section 2 we recall the mathematical properties of the governing equations and fully describe the features of the Riemann problem. In Section 3 we present the new HLLC-type Riemann solver. In Section 4 we carry out a systematic assessment of the solver on a series of carefully chosen local test problems for the states and compare the approximate solutions against available exact solutions. In Section 5 we implement the HLLC solver in the frame of finite volume and DG finite elements. In Section 6 we implement the HLLC solver in the framework of a new variant of path conservative methods for hyperbolic systems in nonconservative form. In Section 7 we systematically assess the performance of the new path-conservative method with the new HLLC solver and compare the results with the HLLC solver used in the finite volume frame work and the DG finite element frameworks. We estimate the CPU time necessary to implement our approximate Riemann solver and compare it with the time needed for the exact solver. Conclusions are drawn in Section 8.

2. Equations and the Riemann problem

The Baer–Nunziato equations are a three-dimensional time-dependent system of 11 equations with source terms. Our ultimate goal is to develop numerical schemes to solve these, using for example finite volume methods. To this end it is helpful to consider the governing equations in the direction normal to a cell boundary to find a numerical flux. Hence, without loss of generality we can consider the x-split equations.

2.1. Split three-dimensional Baer–Nunziato equations

The x-split three-dimensional Baer–Nunziato equations are a set of 11 PDEs:

$$\partial_t \mathbf{Q} + \partial_x \mathbf{F}(\mathbf{Q}) + \mathbf{T}(\mathbf{Q})\partial_x \bar{\alpha} = \mathbf{S}(\mathbf{Q}), \tag{1}$$

where

$$\mathbf{Q}=\begin{bmatrix}\bar{\alpha}\\ \bar{\alpha}\bar{\rho}\\ \bar{\alpha}\bar{\rho}\bar{u}\\ \bar{\alpha}\bar{\rho}\bar{v}\\ \bar{\alpha}\bar{\rho}\bar{w}\\ \bar{\alpha}\bar{\rho}\bar{E}\\ \alpha\rho\\ \alpha\rho u\\ \alpha\rho v\\ \alpha\rho w\\ \alpha\rho E\end{bmatrix},\quad \mathbf{F}(\mathbf{Q})=\begin{bmatrix}0\\ \bar{\alpha}\bar{\rho}\bar{u}\\ \bar{\alpha}(\bar{\rho}\bar{u}^2+\bar{p})\\ \bar{\alpha}\bar{\rho}\bar{u}\bar{v}\\ \bar{\alpha}\bar{\rho}\bar{u}\bar{w}\\ \bar{\alpha}\bar{u}(\bar{\rho}\bar{E}+\bar{p})\\ \alpha\rho u\\ \alpha(\rho u^2+p)\\ \alpha\rho uv\\ \alpha\rho uw\\ \alpha u(\rho E+p)\end{bmatrix},\quad \mathbf{T}(\mathbf{Q})=\begin{bmatrix}\bar{u}\\ 0\\ -p\\ 0\\ 0\\ -p\bar{u}\\ 0\\ p\\ 0\\ 0\\ p\bar{u}\end{bmatrix},\quad \mathbf{S}(\mathbf{Q})=\begin{bmatrix}s_1\\ s_2\\ s_3\\ s_4\\ s_5\\ s_6\\ s_7\\ s_8\\ s_9\\ s_{10}\\ s_{11}\end{bmatrix}.$$

The first six equations for variables with bar relate to the solid phase and the remaining five equations to the gas phase. Here ρ,u,v,w,p,E are gas density, velocity components, pressure and total energy, and $\bar{\rho},\bar{u},\bar{v},\bar{w},\bar{p},\bar{E}$ are the corresponding variables for the solid; α and $\bar{\alpha}$ are volume fractions.

We assume an ideal equation of state (EOS) for the gas phase and a stiffened EOS for the solid phase:

$$p=(\gamma-1)\rho e,$$
$$\bar{p}=(\bar{\gamma}-1)\bar{\rho}\bar{e}-\bar{\gamma}\overline{P}_0,$$

where e and $\bar{e}$ are the specific internal energies, γ and $\bar{\gamma}$ are the specific heat ratios of the gas and solid phases, respectively, and $\overline{P}_0$ is a known constant.

The sound speeds of the gas and solid phases are calculated as follows:

$$a=\sqrt{\frac{\gamma p}{\rho}},\quad \bar{a}=\sqrt{\frac{\bar{\gamma}(\bar{p}+\overline{P}_0)}{\bar{\rho}}}.$$

Solid and gas volume fractions are related through the saturation condition: $\bar{\alpha}+\alpha=1$. In this paper we are primarily interested in the principal part of Eq. (1) and therefore we can take $\mathbf{S}(\mathbf{Q})=\mathbf{0}$, no source terms. Eq. (1) include also the purely one-dimensional Baer–Nunziato equations in the case of no tangential velocities. Therefore the study of split three-dimensional equations is useful both for one-dimensional and multidimensional problems.

2.2. Eigenstructure

In this section we derive the expressions for eigenvalues and eigenvectors of the coefficient matrix of system (1) written in quasilinear form. These are used to describe the behaviour of physical variables across each characteristic field in the Riemann problem. The homogeneous Baer–Nunziato Eq. (1) can be rewritten in the following quasilinear form:

$$\partial_t\mathbf{Q}+\mathbf{A}(\mathbf{Q})\partial_x\mathbf{Q}=\mathbf{0}, \tag{2}$$

where, as before, $\mathbf{Q}$ denotes the vector of conserved variables and the matrix $\mathbf{A}(\mathbf{Q})$ takes the form

$$\mathbf{A}(\mathbf{Q})=\begin{bmatrix}\bar{u}&0&0&0&0&0&0&0&0&0&0\\ 0&0&1&0&0&0&0&0&0&0&0\\ -p-\bar{\gamma}\overline{P}_0&\hat{\bar{\gamma}}\overline{H}-\bar{u}^2-\bar{a}^2&(3-\bar{\gamma})\bar{u}&-\hat{\bar{\gamma}}\bar{v}&-\hat{\bar{\gamma}}\bar{w}&\hat{\bar{\gamma}}&0&0&0&0&0\\ 0&-\bar{u}\bar{v}&\bar{v}&\bar{u}&0&0&0&0&0&0&0\\ 0&-\bar{u}\bar{w}&\bar{w}&0&\bar{u}&0&0&0&0&0&0\\ \bar{u}(-p-\bar{\gamma}\overline{P}_0)&\bar{u}\left[-\overline{H}+\frac{\hat{\bar{\gamma}}\bar{\mathbf{V}}^2}{2}\right]&\overline{H}-\hat{\bar{\gamma}}\bar{u}^2&-\hat{\bar{\gamma}}\bar{u}\bar{v}&-\hat{\bar{\gamma}}\bar{u}\bar{w}&\bar{\gamma}\bar{u}&0&0&0&0&0\\ 0&0&0&0&0&0&0&1&0&0&0\\ p&0&0&0&0&0&\hat{\gamma}H-u^2-a^2&(3-\gamma)u&-\hat{\gamma}v&-\hat{\gamma}w&\hat{\gamma}\\ 0&0&0&0&0&0&-uv&v&u&0&0\\ 0&0&0&0&0&0&-uw&w&0&u&0\\ p\bar{u}&0&0&0&0&0&u\left[-H+\frac{\hat{\gamma}\mathbf{V}^2}{2}\right]&H-\hat{\gamma}u^2&-\hat{\gamma}uv&-\hat{\gamma}&\gamma u\end{bmatrix},$$

with $\hat{\bar{\gamma}}=\bar{\gamma}-1,\hat{\gamma}=\gamma-1,\bar{\mathbf{V}}^2=\bar{u}^2+\bar{v}^2+\bar{w}^2,\mathbf{V}^2=u^2+v^2+w^2;\overline{H}=\overline{E}+\bar{p}/\bar{\rho}=\bar{\mathbf{V}}^2/2+\bar{a}^2/(\bar{\gamma}-1)$ and $H=E+p/\rho=\mathbf{V}^2/2+a^2/(\gamma-1)$ denote solid and gas enthalpies.

The matrix A has 11 eigenvalues

$$\lambda_1 = u - a, \quad \lambda_2 = \lambda_3 = \lambda_4 = u, \quad \lambda_5 = u + a, \quad \lambda_6 = \bar{u} - \bar{a}, \quad \lambda_7 = \lambda_8 = \lambda_9 = \bar{u}, \quad \lambda_{10} = \bar{u} + \bar{a}, \quad \lambda_{11} = \bar{u}$$

and a corresponding set of linearly independent right eigenvectors

$$\mathbf{K}^1 = \begin{bmatrix} 0 \\ 0 \\ 0 \\ 0 \\ 0 \\ 0 \\ 1 \\ u-a \\ v \\ w \\ H-ua \end{bmatrix}, \quad \mathbf{K}^2 = \begin{bmatrix} 0 \\ 0 \\ 0 \\ 0 \\ 0 \\ 0 \\ 1 \\ u \\ 0 \\ 0 \\ u^2 - \frac{\mathbf{V}^2}{2} \end{bmatrix}, \quad \mathbf{K}^3 = \begin{bmatrix} 0 \\ 0 \\ 0 \\ 0 \\ 0 \\ 0 \\ v \\ uv \\ \frac{\mathbf{V}^2}{2} - u^2 \\ 0 \\ 0 \end{bmatrix}, \quad \mathbf{K}^4 = \begin{bmatrix} 0 \\ 0 \\ 0 \\ 0 \\ 0 \\ 0 \\ w \\ uw \\ 0 \\ \frac{\mathbf{V}^2}{2} - u^2 \\ 0 \end{bmatrix}, \quad \mathbf{K}^5 = \begin{bmatrix} 0 \\ 0 \\ 0 \\ 0 \\ 0 \\ 0 \\ 1 \\ u+a \\ v \\ w \\ H+ua \end{bmatrix},$$

$$\mathbf{K}^6 = \begin{bmatrix} 0 \\ 1 \\ \bar{u} - \bar{a} \\ \bar{v} \\ \bar{w} \\ \overline{H} - \bar{u}\bar{a} \\ 0 \\ 0 \\ 0 \\ 0 \\ 0 \end{bmatrix}, \quad \mathbf{K}^7 = \begin{bmatrix} 0 \\ 1 \\ \bar{u} \\ 0 \\ 0 \\ \bar{u}^2 - \frac{\bar{\mathbf{V}}^2}{2} \\ 0 \\ 0 \\ 0 \\ 0 \\ 0 \end{bmatrix}, \quad \mathbf{K}^8 = \begin{bmatrix} 0 \\ \bar{v} \\ \bar{u}\bar{v} \\ \frac{\bar{\mathbf{V}}^2}{2} - \bar{u}^2 \\ 0 \\ 0 \\ 0 \\ 0 \\ 0 \\ 0 \\ 0 \end{bmatrix}, \quad \mathbf{K}^9 = \begin{bmatrix} 0 \\ \bar{w} \\ \bar{u}\bar{w} \\ 0 \\ \frac{\bar{\mathbf{V}}^2}{2} - \bar{u}^2 \\ 0 \\ 0 \\ 0 \\ 0 \\ 0 \\ 0 \end{bmatrix}, \quad \mathbf{K}^{10} = \begin{bmatrix} 0 \\ 1 \\ \bar{u} + \bar{a} \\ \bar{v} \\ \bar{w} \\ \overline{H} + \bar{u}\bar{a} \\ 0 \\ 0 \\ 0 \\ 0 \\ 0 \end{bmatrix},$$

$$\mathbf{K}^{11} = \begin{bmatrix} (\bar{\gamma}-1)(a^2 - (u-\bar{u})^2)\left(\frac{\bar{\mathbf{V}}^2}{2} - \bar{u}^2\right) \\ (p + \bar{\gamma}\overline{P}_0)(a^2 - (u-\bar{u})^2) \\ \bar{u}(p + \bar{\gamma}\overline{P}_0)(a^2 - (u-\bar{u})^2) \\ 0 \\ 0 \\ 0 \\ \gamma(\bar{\gamma}-1)p\left(\bar{u}^2 - \frac{\bar{\mathbf{V}}^2}{2}\right) \\ \gamma(\bar{\gamma}-1)p\bar{u}\left(\bar{u}^2 - \frac{\bar{\mathbf{V}}^2}{2}\right) \\ \gamma(\bar{\gamma}-1)pv\left(\bar{u}^2 - \frac{\bar{\mathbf{V}}^2}{2}\right) \\ \gamma(\bar{\gamma}-1)pw\left(\bar{u}^2 - \frac{\bar{\mathbf{V}}^2}{2}\right) \\ \frac{\bar{\gamma}-1}{\gamma-1}p\left[a^2 - \frac{\gamma-1}{2}\left((\gamma-2)(u-\bar{u})^2 - \gamma(u^2-\bar{u}^2) - \gamma\mathbf{V}^2\right)\right]\left(\bar{u}^2 - \frac{\bar{\mathbf{V}}^2}{2}\right) \end{bmatrix}.$$

We note that the expressions for right eigenvectors of the system written in conservative variables are also useful, for example, in constructing of slope limiters for high-order methods like the DG method considered in this paper. See [23] for details.

The Baer–Nunziato equations may be also written in physical (or primitive) variables, namely

$$\mathbf{W} = [\bar{\alpha}, \bar{\rho}, \bar{u}, \bar{v}, \bar{w}, \bar{p}, \rho, u, v, w, p]^T$$

in nonconservative form

$$\partial_t \mathbf{W} + \mathbf{B}(\mathbf{W})\partial_x \mathbf{W} = 0. \tag{3}$$

In this case the matrix $\mathbf{B}(\mathbf{W})$ takes the form

$$\mathbf{B} = \begin{bmatrix} \bar{u} & 0 & 0 & 0 & 0 & 0 & 0 & 0 & 0 & 0 & 0 \\ 0 & \bar{u} & \bar{\rho} & 0 & 0 & 0 & 0 & 0 & 0 & 0 & 0 \\ -\frac{\Delta p}{\alpha\bar{\rho}} & 0 & \bar{u} & 0 & 0 & \frac{1}{\bar{\rho}} & 0 & 0 & 0 & 0 & 0 \\ 0 & 0 & 0 & \bar{u} & 0 & 0 & 0 & 0 & 0 & 0 & 0 \\ 0 & 0 & 0 & 0 & \bar{u} & 0 & 0 & 0 & 0 & 0 & 0 \\ 0 & 0 & \bar{\rho}\bar{a}^2 & 0 & 0 & \bar{u} & 0 & 0 & 0 & 0 & 0 \\ -\frac{\rho\Delta u}{\alpha} & 0 & 0 & 0 & 0 & 0 & u & \rho & 0 & 0 & 0 \\ 0 & 0 & 0 & 0 & 0 & 0 & 0 & u & 0 & 0 & \frac{1}{\rho} \\ 0 & 0 & 0 & 0 & 0 & 0 & 0 & 0 & u & 0 & 0 \\ 0 & 0 & 0 & 0 & 0 & 0 & 0 & 0 & 0 & u & 0 \\ -\frac{\rho a^2\Delta u}{\alpha} & 0 & 0 & 0 & 0 & 0 & 0 & \rho a^2 & 0 & 0 & u \end{bmatrix}.$$

The eigenvalues of the matrix $\mathbf{B}(\mathbf{W})$ are the values below

$$\lambda_1 = u - a, \quad \lambda_2 = \lambda_3 = \lambda_4 = u, \quad \lambda_5 = u + a, \quad \lambda_6 = \bar{u} - \bar{a}, \quad \lambda_7 = \lambda_8 = \lambda_9 = \bar{u}, \quad \lambda_{10} = \bar{u} + \bar{a}, \quad \lambda_{11} = \bar{u}$$

and the right eigenvectors corresponding to these eigenvalues are

$$\mathbf{K}^1 = \begin{bmatrix} 0 \\ 0 \\ 0 \\ 0 \\ 0 \\ 0 \\ \rho \\ -a \\ 0 \\ 0 \\ \rho a^2 \end{bmatrix}, \quad \mathbf{K}^2 = \begin{bmatrix} 0 \\ 0 \\ 0 \\ 0 \\ 0 \\ 0 \\ 1 \\ 0 \\ 0 \\ 0 \\ 0 \end{bmatrix}, \quad \mathbf{K}^3 = \begin{bmatrix} 0 \\ 0 \\ 0 \\ 0 \\ 0 \\ 0 \\ 0 \\ 0 \\ 1 \\ 0 \\ 0 \end{bmatrix}, \quad \mathbf{K}^4 = \begin{bmatrix} 0 \\ 0 \\ 0 \\ 0 \\ 0 \\ 0 \\ 0 \\ 0 \\ 0 \\ 1 \\ 0 \end{bmatrix}, \quad \mathbf{K}^5 = \begin{bmatrix} 0 \\ 0 \\ 0 \\ 0 \\ 0 \\ 0 \\ \rho \\ a \\ 0 \\ 0 \\ \rho a^2 \end{bmatrix}, \tag{4}$$

$$\mathbf{K}^6 = \begin{bmatrix} 0 \\ \bar{\rho} \\ -\bar{a} \\ 0 \\ 0 \\ \bar{\rho}\bar{a}^2 \\ 0 \\ 0 \\ 0 \\ 0 \\ 0 \end{bmatrix}, \quad \mathbf{K}^7 = \begin{bmatrix} 0 \\ 1 \\ 0 \\ 0 \\ 0 \\ 0 \\ 0 \\ 0 \\ 0 \\ 0 \\ 0 \end{bmatrix}, \quad \mathbf{K}^8 = \begin{bmatrix} 0 \\ 0 \\ 0 \\ 1 \\ 0 \\ 0 \\ 0 \\ 0 \\ 0 \\ 0 \\ 0 \end{bmatrix}, \quad \mathbf{K}^9 = \begin{bmatrix} 0 \\ 0 \\ 0 \\ 0 \\ 1 \\ 0 \\ 0 \\ 0 \\ 0 \\ 0 \\ 0 \end{bmatrix}, \quad \mathbf{K}^{10} = \begin{bmatrix} 0 \\ \bar{\rho} \\ \bar{a} \\ 0 \\ 0 \\ \bar{\rho}\bar{a}^2 \\ 0 \\ 0 \\ 0 \\ 0 \\ 0 \end{bmatrix}, \tag{5}$$

$$\mathbf{K}^{11} = \begin{bmatrix} 1 \\ 0 \\ 0 \\ 0 \\ 0 \\ \frac{\Delta p}{\alpha} \\ -\frac{\rho(\Delta u)^2}{\alpha(a^2-(\Delta u)^2)} \\ \frac{a^2\Delta u}{\alpha(a^2-(\Delta u)^2)} \\ 0 \\ 0 \\ -\frac{\rho a^2(\Delta u)^2}{\alpha(a^2-(\Delta u)^2)} \end{bmatrix}, \tag{6}$$

where $\Delta p = p - \bar{p}$ and $\Delta u = u - \bar{u}$.

2.3. Exact solution of the Riemann problem

Consider the Riemann problem for the homogeneous Baer–Nunziato equations, namely

$$\partial_t \mathbf{Q} + \partial_x \mathbf{F}(\mathbf{Q}) + \mathbf{T}(\mathbf{Q})\partial_x \bar{\alpha} = \mathbf{0}, \tag{7}$$

$$\mathbf{Q}(x,0) = \begin{cases} \mathbf{Q}_L(x), & \text{if } x < 0; \\ \mathbf{Q}_R(x), & \text{if } x > 0. \end{cases} \tag{8}$$

Examination of the right eigenvectors of the system in physical variables (4)–(6) with generalized Riemann invariants [18] in the appropriate characteristic fields allows us to describe the structure of the exact solution of the Riemann problem (7) and (8). A variable corresponding to a zero component of the ith eigenvector does not change across the ith characteristic field. Recall that the system (3) has 11 eigenvalues, some of which coalesce, and as a result it has six distinct characteristic fields, across which the following relations for the jumps of physical variables are valid:

1. $\lambda_1 = u - a$ (gaseous left nonlinear wave). Solid phase: $d\bar{\alpha} = 0, d\bar{\rho} = 0, d\bar{u} = 0, d\bar{v} = 0, d\bar{w} = 0, d\bar{p} = 0$. Gas phase: $d\alpha = 0$, $dv = 0, dw = 0$.
2. $\lambda_2 = u$ (gaseous contact). Solid phase: $d\bar{\alpha} = 0, d\bar{\rho} = 0, d\bar{u} = 0, d\bar{v} = 0, d\bar{w} = 0, d\bar{p} = 0$. Gas phase: $d\alpha = 0, du = 0, dp = 0$.
3. $\lambda_3 = u + a$ (gaseous right nonlinear wave). Solid phase: $d\bar{\alpha} = 0, d\bar{\rho} = 0, d\bar{u} = 0, d\bar{v} = 0, d\bar{w} = 0, d\bar{p} = 0$. Gas phase: $d\alpha = 0, dv = 0, dw = 0$.
4. $\lambda_4 = \bar{u} - \bar{a}$ (solid left nonlinear wave). Solid phase: $d\bar{\alpha} = 0, d\bar{v} = 0, d\bar{w} = 0$. Gas phase: $d\alpha = 0, d\rho = 0$, $du = 0, dv = 0, dw = 0, dp = 0$.
5. $\lambda_5 = \bar{u}$ (solid contact). Solid phase: $d\bar{u} = 0$. Gas phase: $dv = 0, dw = 0$.
6. $\lambda_6 = \bar{u} + \bar{a}$ (solid right nonlinear wave). Solid phase: $d\bar{\alpha} = 0, d\bar{v} = 0, d\bar{w} = 0$. Gas phase: $d\alpha = 0, d\rho = 0$, $du = 0, dv = 0, dw = 0, dp = 0$.

Using these relations we can conclude that all solid phase variables remain constant across the three gaseous characteristic fields, while the solid contact changes all gaseous variables except for the tangential velocities. The left and right solid nonlinear waves do not affect the gaseous-phase variables. The resulting structure of the exact solution is illustrated in Fig. 1. There are in general six distinct wave families: three for the gas phase and three for the solid phase. These six waves separate seven constant states. In Fig. 1 we denote the gaseous variables by $\mathbf{U}$ and the solid variables by $\bar{\mathbf{U}}$, except for the volume fraction $\bar{\alpha}$, which is presented separately, where

$$\bar{\mathbf{U}} = [\bar{\alpha}\bar{\rho}, \bar{\alpha}\bar{\rho}\bar{u}, \bar{\alpha}\bar{\rho}\bar{v}, \bar{\alpha}\bar{\rho}\bar{w}, \bar{\alpha}\bar{\rho}\bar{E}]^T; \quad \mathbf{U} = [\alpha\rho, \alpha\rho u, \alpha\rho v, \alpha\rho w, \alpha\rho E]^T.$$

Consider Figs. 2 and 3. These illustrate in more detail the features of the intermediate waves. For the solid phase there are two intermediate regions of constant states "$*L$" and "$*R$" separated by the solid contact, in which densities and pressures are different and x-velocities are equal: $\bar{u}^*_L = \bar{u}^*_R$. For the gas phase the intermediate values are presented by three constant regions, denoted by "$*L$", "$*0$" and "$*R$". The exact values for these states are in general dependent on the relative positions of the two contact waves. For the configuration in Fig. 3 we have the following definitions of the variables in region "$*0$":

$$u^*_0 = u^*_R, \quad p^*_0 = p^*_R, \quad \rho^*_0 = \rho^*_L \left(\frac{p^*_R}{p^*_L}\right)^{1/\gamma}.$$

Expressions for $\bar{\rho}^*_L, \bar{u}^*_L, \bar{p}^*_L, \bar{\rho}^*_R, \bar{u}^*_R, \bar{p}^*_R$ and $\rho^*_L, u^*_L, p^*_L, \rho^*_R, u^*_R, p^*_R$ can be obtained by considering the Rankine–Hugoniot conditions across the appropriate nonlinear wave [18].

The tangential velocities $\bar{v}, \bar{w}, v$ and w do not change across the left and right nonlinear waves of each phase, the jump of this quantities occurs across the contact discontinuity of the corresponding phase and is defined only by the left and right

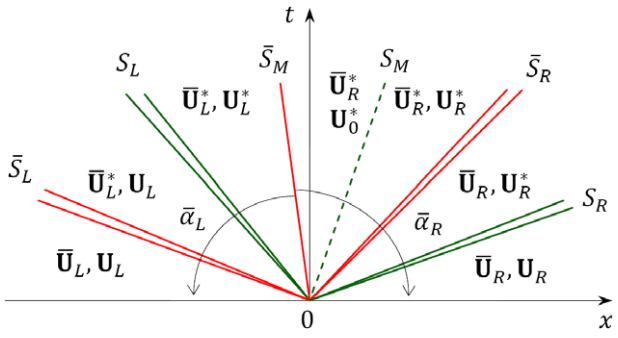

Fig. 1. Structure of the exact solution of the Riemann problem for the homogeneous Baer–Nunziato equations.

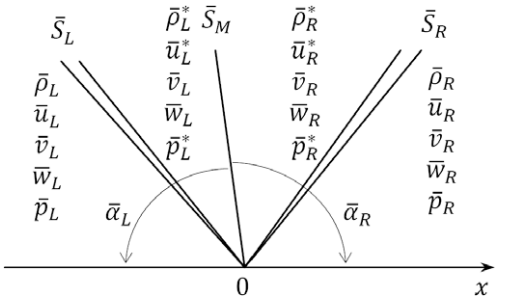

Fig. 2. Intermediate states for solid phase (split 3D case).

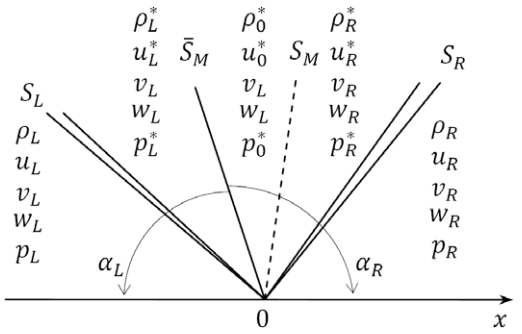

Fig. 3. Intermediate states for gas phase (split 3D case).

initial data. The solution of the Riemann problem for the split three-dimensional Baer–Nunziato equations is therefore basically the same as for one-dimensional equations. In what follows we derive the Riemann solver applicable for one-dimensional and split two- and three-dimensional problems and estimate its performance on several specially chosen test cases.

An important property of Baer–Nunziato equations is the fact that the jump of the solid phase volume fraction occurs only across the solid contact discontinuity, which means that the two phases remain decoupled away from the solid contact, and Eq. (1) reduce to a pair of Euler equations for each phase separately. In the vicinity of the solid contact the phases become coupled due to the change of volume fractions, and additional relations connecting the states on either side of the solid contact must be considered. A special approximation of this solid contact discontinuity as a thin layer was proposed by Schwendeman et al. in [9]. In that paper the thin-layer equations across the solid contact were derived and solved numerically.

3. An HLLC-type Riemann solver

In this section we estimate the intermediate values of the solution of the Riemann problem (see Figs. 2 and 3) using the HLLC approach. In what follows we consider the purely one-dimensional version of the Eq. (1), leaving the tangential velocities out of consideration and therefore dealing with the system of 7 equations with respect to conservative variables vector

$$\mathbf{Q} = [\bar{\alpha}, \bar{\alpha}\bar{\rho}, \bar{\alpha}\bar{\rho}\bar{u}, \bar{\alpha}\bar{\rho}\bar{E}, \alpha\rho, \alpha\rho u, \alpha\rho E]^T.$$

We assume that wave speed estimates $\bar{S}_L, S_L, \bar{S}_R, S_R$ are available. The solver takes into account the behaviour of the solution across the nonlinear waves of speeds $\bar{S}_L, S_L, \bar{S}_R, S_R$ and the behaviour of the solution across the contact waves of speeds $\bar{S}_M, S_M$. We first deal with the $\bar{S}_M$ wave.

3.1. Thin layer equations

We follow the basic ideas of Schwendeman et al. [9] in construction of our approximate numerical flux, in particular, we consider the thin-layer equations across the contact discontinuity in the solid phase. Two different configurations of the characteristic fields are possible for the Baer–Nunziato equations, depending on the values of the relative velocity $u - \bar{u}$: the "subsonic" case, for which the relation $(u - \bar{u})^2 < a^2$ is satisfied, and the "supersonic" case, for which the opposite condition $(u - \bar{u})^2 > a^2$ holds true.

In this paper we deal only with the "subsonic" situation, which is considered to be more relevant [9]. In this model the solid contact is situated between the left and right gas-phase waves on the wave pattern in $x - t$ plane. There are two possible "subsonic" wave configurations: one of them is presented in Figs. 2 and 3, where the solid contact lies to the left of the

gas contact. Another possible "subsonic" wave configuration corresponds to the case when the solid contact is situated on the right of the gas contact.

For the "subsonic" case illustrated in Figs. 2 and 3 the thin-layer equations take the following form:

$$\begin{aligned}
&\bar{u}_R^* - \bar{u}_L^* = 0;\\
&\alpha_R \left(\frac{p_R^*}{p_L^*}\right)^{1/\gamma} (u_R^* - \bar{u}_R^*) - \alpha_L (u_L^* - \bar{u}_L^*) = 0;\\
&\bar{\alpha}_R \bar{p}_R^* + \alpha_R p_R^* - \bar{\alpha}_L \bar{p}_L^* - \alpha_L p_L^* + \alpha_L \rho_L^* (u_L^* - \bar{u}_L^*)(u_R^* - u_L^*) = 0;\\
&\frac{\gamma p_R^*}{(\gamma-1)\rho_L^*} \left(\frac{p_L^*}{p_R^*}\right)^{1/\gamma} + \frac{1}{2}(u_R^* - \bar{u}_R^*)^2 - \frac{\gamma p_L^*}{(\gamma-1)\rho_L^*} - \frac{1}{2}(u_L^* - \bar{u}_L v)^2 = 0.
\end{aligned} \tag{9}$$

For the derivation of this system see [9]. In this paper the solid contact wave is treated as a smooth layer of infinitesimal width and the governing equations across this wave are thus rewritten in terms of the independent variable $\xi = x - Ut$, where U is the speed of the solid contact:

$$-U\mathbf{Q}_\xi + \mathbf{F}_\xi(\mathbf{Q}) + \mathbf{T}(\mathbf{Q})\bar{\alpha}_\xi = 0. \tag{10}$$

Considering Eq. (10) componentwise we can obtain the following system:

$$\begin{aligned}
&U = \bar{u};\\
&(\bar{\alpha}\bar{\rho})_\xi = p\bar{\alpha}_\xi;\\
&-\bar{u}(\alpha\rho)_\xi + (\alpha\rho u)_\xi = 0;\\
&-\bar{u}(\alpha\rho u)_\xi + (\alpha\rho u^2 + \alpha p)_\xi = -p\bar{\alpha}_\xi;\\
&-\bar{u}(\alpha\rho E)_\xi + (\alpha\rho u E + \alpha u p)_\xi = -p\bar{u}\bar{\alpha}_\xi,
\end{aligned} \tag{11}$$

which leads to a set of jump conditions

$$\begin{aligned}
&\alpha\rho(u - \bar{u}) = K_1;\\
&\alpha\rho(u - \bar{u})^2 + \alpha p + \bar{\alpha}\bar{p} = K_2;\\
&h + \frac{1}{2}(u - \bar{u})^2 = K_3,
\end{aligned} \tag{12}$$

where $h = e + p/\rho$ is the enthalpy of the gas and K_1, K_2, K_3 are constants of integration.

Direct application of the jump conditions (12) across the solid contact results in the thin-layer Eqs. (9).

We note that the same system of Eq. (9) can be obtained by considering the generalized Rankine–Hugoniot conditions across the solid contact wave. Assume that there exists a function $\widetilde{\mathbf{F}}(\mathbf{Q})$ such that

$$\widetilde{\mathbf{F}}(\mathbf{Q}) = \frac{\partial \widetilde{\mathbf{T}}(\mathbf{Q})}{\partial \mathbf{Q}},$$

where $\widetilde{\mathbf{T}}(\mathbf{Q}) = [\mathbf{T}(\mathbf{Q}), \mathbf{0}, \ldots, \mathbf{0}]$.

Then using the flux vector $\mathbf{H} = \mathbf{F} + \widetilde{\mathbf{F}}$ we can rewrite Eq. (1) in the conservative form

$$\partial_t \mathbf{Q} + \partial_x \mathbf{H}(\mathbf{Q}) = \mathbf{0}$$

and apply the generalized Rankine–Hugoniot conditions in the form

$$\mathbf{H}_0 - \mathbf{H}_1 = \overline{S}_M(\mathbf{Q}_0 - \mathbf{Q}_1). \tag{13}$$

Taking into account the definition for the flux $\mathbf{H}$ and using the theory reported in [25] for the nonconservative part of the system, namely,

$$\mathbf{N} = \widetilde{\mathbf{F}}_0 - \widetilde{\mathbf{F}}_1 = \int_0^1 \widetilde{\mathbf{T}}(\varphi(s, \mathbf{Q}_1, \mathbf{Q}_0)) \frac{\partial \varphi}{\partial s} ds,$$

where φ is the path satisfying the conditions

$$\begin{aligned}
&\bar{\varphi} : [0,1] \times \mathbf{R}^n \times \mathbf{R}^n \to \mathbf{R}^n,\\
&\bar{\varphi}(0, \mathbf{Q}_1, \mathbf{Q}_0) = \mathbf{Q}_1, \bar{\varphi}(1, \mathbf{Q}_1, \mathbf{Q}_0) = \mathbf{Q}_0,
\end{aligned}$$

we can rewrite (13) as follows:

$$\mathbf{F}_0 - \mathbf{F}_1 + \mathbf{N} = \overline{S}_M(\mathbf{Q}_0 - \mathbf{Q}_1). \tag{14}$$

A straightforward manipulation of the Eq. (14) leads to the jump conditions

$$
\begin{aligned}
&\bar{S}_M = \bar{u}_R^* = \bar{u}_L^*;\\
&\alpha_R\rho_0^*(u_R^* - \bar{S}_M) = \alpha_L\rho_L^*(u_L^* - \bar{S}_M);\\
&\alpha_R\rho_0^* u_R^*(u_R^* - \bar{S}_M) + \alpha_R p_R^* + \bar{\alpha}_R\bar{p}_R^* = \alpha_L\rho_L^* u_L^*(u_L^* - \bar{S}_M) + \alpha_L p_L^* + \bar{\alpha}_L\bar{p}_L^*;\\
&\alpha_R\rho_0^* E_0^*(u_R^* - \bar{S}_M) + \alpha_R u_R^* p_R^* + \bar{\alpha}_R\bar{u}_R^*\bar{p}_R^* = \alpha_L\rho_L^* E_L^*(u_L^* - \bar{S}_M) + \alpha_L u_L^* p_L^* + \bar{\alpha}_L\bar{u}_L^*\bar{p}_L^*,
\end{aligned}
\tag{15}
$$

which are obviously equivalent to the thin-layer equation (9).

The generalized Rankine–Hugoniot conditions (14) also give the definition for the nonconservative term **N**:

$$
\mathbf{N} = \begin{bmatrix}
\bar{S}_M(\bar{\alpha}_R - \bar{\alpha}_L)\\
0\\
-\left(\bar{\alpha}_R\bar{p}_R^* - \bar{\alpha}_L\bar{p}_L^*\right)\\
-\left(\bar{\alpha}_R\bar{u}_R^*\bar{p}_R^* - \bar{\alpha}_L\bar{u}_L^*\bar{p}_L^*\right)\\
0\\
\bar{\alpha}_R\bar{p}_R^* - \bar{\alpha}_L\bar{p}_L^*\\
\bar{\alpha}_R\bar{u}_R^*\bar{p}_R^* - \bar{\alpha}_L\bar{u}_L^*\bar{p}_L^*,
\end{bmatrix},
\tag{16}
$$

which can be used in numerical methods to approximate the term $\mathbf{T}(\mathbf{Q})$.

For another type of "subsonic" wave configuration, when the solid contact lies to the right of gas contact, the thin-layer equations can be written as:

$$
\begin{aligned}
&\bar{u}_R^* - \bar{u}_L^* = 0;\\
&\alpha_R(u_R^* - \bar{u}_R^*) - \alpha_L\left(\frac{p_L^*}{p_R^*}\right)^{1/\gamma}(u_L^* - \bar{u}_L^*) = 0;\\
&\bar{\alpha}_R\bar{p}_R^* + \alpha_R p_R^* - \bar{\alpha}_L\bar{p}_L^* - \alpha_L p_L^* + \alpha_R\rho_R^*(p_R^*)(u_R^* - \bar{u}_R^*)(u_R^* - u_L^*) = 0;\\
&\frac{\gamma p_R^*}{(\gamma-1)\rho_R^*(p_L^*)} + \frac{1}{2}(u_R^* - \bar{u}_R^*)^2 - \frac{\gamma p_L^*}{(\gamma-1)\rho_R^*}\left(\frac{p_R^*}{p_L^*}\right)^{1/\gamma} - \frac{1}{2}(u_L^* - \bar{u}_L^*)^2 = 0.
\end{aligned}
\tag{17}
$$

Recall that in the exact Riemann solver of [9] the nonlinear systems (9) and (17) are considered as systems of four equations for four unknowns $p_L^*, p_R^*, \bar{p}_L^*, \bar{p}_R^*$, and corresponding velocities and densities are related to appropriate pressures and left and right states through nonlinear dependences arising from the analysis of the left and right wave structures. For example, to connect the values u_L^* and p_L^* one needs to analyse the type of the left wave, i.e. define whether it is a shock or a rarefaction wave. Then, one must choose the appropriate expression for the function across this wave:

$$
F_L(p_L^*) = \begin{cases}
(p_L^* - p_L)\left[\frac{A_L}{p_1 + B_L}\right]^{\frac{1}{2}}, & p_L^* > p_L \text{ (shock wave)};\\
\frac{2a_L}{\gamma-1}\left[\left(\frac{p_L^*}{p_L}\right)^{(\gamma-1)/2\gamma} - 1\right], & p_1 < p_L, \text{ (rarefaction)},
\end{cases}
\tag{18}
$$

where $A_L = \frac{2}{(\gamma+1)\rho_L}, B_L = \frac{\gamma-1}{\gamma+1}p_L$, and write the final expression for the velocity:

$$
u_L^* = u_L - F_L(p_L^*).
\tag{19}
$$

Such analysis of the wave structure must be carried out on every step of the iterative solution process of the nonlinear system (9) or (17), with Jacobi matrices dependent on the particular wave type.

3.2. HLLC-type intermediate states

We propose the following simplification of the solution procedure: we combine the HLLC approach [18–22] with the numerical solution of thin-layer equations across solid contact. Instead of analysing the type of left and right waves for each phase we estimate their speeds and use these to connect the states in regions "L" and "$^*L$" (and "R" and "$^*R$", respectively). After that we can use the values computed by HLLC scheme to solve the thin-layer equations.

Consider the "subsonic" wave structure presented in Figs. 2 and 3 separately for solid and gas phases. We treat the left and right waves of each phase as discontinuities propagating with known velocities $\bar{S}_L, \bar{S}_R, S_L$ and S_R, respectively. As mentioned above, there is no change of phase volume fractions across these waves, therefore the two-phase equations reduce to a pair of Euler equations, for which the following averaged Rankine–Hugoniot conditions are valid:

$$
\begin{aligned}
&\bar{\mathbf{G}}_L^* = \bar{\mathbf{G}}_L + \bar{S}_L(\bar{\mathbf{U}}_L^* - \bar{\mathbf{U}}_L),\\
&\bar{\mathbf{G}}_R^* = \bar{\mathbf{G}}_R + \bar{S}_R(\bar{\mathbf{U}}_R^* - \bar{\mathbf{U}}_R),
\end{aligned}
\tag{20}
$$

$$
\begin{aligned}
&\mathbf{G}_L^* = \mathbf{G}_L + S_L(\mathbf{U}_L^* - \mathbf{U}_L),\\
&\mathbf{G}_R^* = \mathbf{G}_R + S_R(\mathbf{U}_R^* - \mathbf{U}_R),
\end{aligned}
\tag{21}
$$

where the states $\bar{\mathbf{U}}_L, \bar{\mathbf{U}}_R, \bar{\mathbf{U}}_L^*, \bar{\mathbf{U}}_R^*, \mathbf{U}_L, \mathbf{U}_R, \mathbf{U}_L^*, \mathbf{U}_R^*$ are presented in Fig. 1 and $\bar{\mathbf{G}}_L, \bar{\mathbf{G}}_R, \mathbf{G}_L, \mathbf{G}_R$ are components of the flux vector $\mathbf{F}$ in (1) corresponding to left and right states:

$$\bar{\mathbf{G}}_L = \bar{\mathbf{G}}(\bar{\mathbf{U}}_L), \quad \bar{\mathbf{G}}_R = \bar{\mathbf{G}}(\bar{\mathbf{U}}_R);$$
$$\mathbf{G}_L = \mathbf{G}(\mathbf{U}_L), \quad \mathbf{G}_R = \mathbf{G}(\mathbf{U}_R),$$

where

$$\bar{\mathbf{G}} = [\bar{\alpha}\bar{\rho}\bar{u}, \bar{\alpha}(\bar{\rho}\bar{u}^2 + \bar{p}), \bar{\alpha}\bar{u}(\bar{\rho}\bar{E} + \bar{p})]^T;$$
$$\mathbf{G} = [\alpha\rho u, \alpha(\rho u^2 + p), \alpha u(\rho E + p)]^T.$$

From Eqs. (20) and (21) we can obtain direct expressions for the intermediate states:

$$\bar{\rho}_L^*(\bar{u}_L^*) = \bar{\rho}_L\left(\frac{\bar{S}_L - \bar{u}_L}{\bar{S}_L - \bar{u}_L^*}\right), \tag{22}$$
$$\bar{p}_L^*(\bar{u}_L^*) = \bar{p}_L + \bar{\rho}_L(\bar{S}_L - \bar{u}_L)(\bar{u}_L^* - \bar{u}_L),$$
$$\bar{\rho}_R^*(\bar{u}_R^*) = \bar{\rho}_R\left(\frac{\bar{S}_R - \bar{u}_R}{\bar{S}_R - \bar{u}_R^*}\right), \tag{23}$$
$$\bar{p}_R^*(\bar{u}_R^*) = \bar{p}_R + \bar{\rho}_R(\bar{S}_R - \bar{u}_R)(\bar{u}_R^* - \bar{u}_R).$$

Analogous expressions are valid for "$*L$" and "$*R$" states in the gas phase if we have the wave speeds estimates S_L and S_R:

$$\rho_L^*(u_L^*) = \rho_L\left(\frac{S_L - u_L}{S_L - u_L^*}\right), \tag{24}$$
$$p_L^*(u_L^*) = p_L + \rho_L(S_L - u_L)(u_L^* - u_L),$$
$$\rho_R^*(u_R^*) = \rho_R\left(\frac{S_R - u_R}{S_R - u_R^*}\right), \tag{25}$$
$$p_R^*(u_R^*) = p_R + \rho_R(S_R - u_R)(u_R^* - u_R).$$

Note that in Eqs. (24) and (25) the gas velocities u_L^* and u_R^* can be different, unlike the classical Euler equations.

3.3. Resulting nonlinear system

For the solution of the "subsonic" nonlinear thin-layer equations across the solid contact we choose the four pressures $p_L^*, p_R^*, \bar{p}_L^*, \bar{p}_R^*$ as independent variables and express the velocities and densities of both phases in terms of these pressures from HLLC relations (22) and (25), that is for $K = L, R$

$$\bar{u}_K^*(\bar{p}_K^*) = \bar{u}_K + \frac{\bar{p}_K^* - \bar{p}_K}{\bar{\rho}_K\left(\bar{S}_R - \bar{u}_K\right)}, \tag{26}$$

$$\bar{\rho}_K^*(\bar{p}_K^*) = \bar{\rho}_K^*\left(\frac{\bar{S}_K - \bar{u}_K}{\bar{S}_K - \bar{u}_K^*(\bar{p}_K^*)}\right) = \frac{\bar{\rho}_K^2\left(\bar{S}_K - \bar{u}_K\right)^2}{\bar{\rho}_K\left(\bar{S}_K - \bar{u}_K\right)^2 - (\bar{p}_K^* - \bar{p}_K)} \tag{27}$$

for the solid phase, and

$$u_K^*(p_K^*) = u_K + \frac{p_K^* - p_K}{\rho_K(S_R - u_K)}, \tag{28}$$

$$\rho_K^*(p_K^*) = \rho_K^*\left(\frac{S_K - u_K}{S_K - u_K^*(p_K^*)}\right) = \frac{\rho_K^2(S_K - u_K)^2}{\rho_K(S_K - u_K)^2 - (p_K^* - p_K)} \tag{29}$$

for the gas phase.

Substituting the expressions (26)–(29) in Eq. (9) or (17) we finally obtain the nonlinear system

$$\begin{aligned}
&\bar{u}_R^*(\bar{p}_R^*) - \bar{u}_L^*(\bar{p}_L^*) = 0;\\
&\alpha_R\left(\frac{p_R^*}{p_L^*}\right)^{1/\gamma}(u_R^*(p_R^*) - \bar{u}_R^*(\bar{p}_R^*)) - \alpha_L(u_L^*(p_L^*) - \bar{u}_L^*(\bar{p}_L^*)) = 0;\\
&\alpha_L\rho_L^*(p_L^*)(u_L^*(p_L^*) - \bar{u}_L^*(\bar{p}_L^*))(u_R^*(p_R^*) - u_L^*(p_L^*)) + \bar{\alpha}_R\bar{p}_R^* + \alpha_R p_R^* - \bar{\alpha}_L\bar{p}_L^* - \alpha_L p_L^* = 0;\\
&\frac{\gamma p_R^*}{(\gamma-1)\rho_L^*(p_L^*)}\left(\frac{p_L^*}{p_R^*}\right)^{1/\gamma} + \frac{1}{2}(u_R^*(p_R^*) - \bar{u}_R^*(\bar{p}_R^*))^2 - \frac{\gamma p_L^*}{(\gamma-1)\rho_L^*(p_L^*)} - \frac{1}{2}(u_L^*(p_L^*) - \bar{u}_L^*(\bar{p}_L^*))^2 = 0
\end{aligned} \tag{30}$$

for the wave configuration in Figs. 2 and 3, or

$$
\begin{aligned}
&\bar{u}_R^*(\bar{p}_R^*) - \bar{u}_L^*(\bar{p}_L^*) = 0;\\
&\alpha_R\left(u_R^*(p_R^*) - \bar{u}_R^*(\bar{p}_R^*)\right) - \alpha_L\left(\frac{p_L^*}{p_R^*}\right)^{1/\gamma}\left(u_L^*(p_L^*) - \bar{u}_L^*(\bar{p}_L^*)\right) = 0;\\
&\alpha_R\rho_R^*(p_R^*)\left(u_R^*(p_R^*) - \bar{u}_R^*(\bar{p}_R^*)\right)\left(u_R^*(p_R^*) - u_L^*(p_L^*)\right) + \bar{\alpha}_R\bar{p}_R^* + \alpha_R p_R^* - \bar{\alpha}_L\bar{p}_L^* - \alpha_L p_L^* = 0;\\
&\frac{\gamma p_R^*}{(\gamma-1)\rho_R^*(p_L^*)} + \frac{1}{2}\left(u_R^*(p_R^*) - \bar{u}_R^*(\bar{p}_R^*)\right)^2 - \frac{\gamma p_L^*}{(\gamma-1)\rho_R^*(p_R^*)}\left(\frac{p_R^*}{p_L^*}\right)^{1/\gamma} - \frac{1}{2}\left(u_L^*(p_L^*) - \bar{u}_L^*(\bar{p}_L^*)\right)^2 = 0
\end{aligned}
\tag{31}
$$

for the other "subsonic" wave pattern.

We use Newton's method to solve the appropriate nonlinear system to obtain the pressures $p_L^*, p_R^*, \bar{p}_L^*, \bar{p}_R^*$. Note that we do not need to know the estimates for the velocities of the intermediate gas and solid contact waves, as these are included in the resulting nonlinear system. All the other quantities are then computed using (26)–(29) and relations for the values in region "*0":

$$
\begin{aligned}
&\rho_0^* = \rho_L^*\left(\frac{p_R^*}{p_L^*}\right)^{1/\gamma},\\
&u_0^* = u_R^*,\\
&p_0^* = p_R^*
\end{aligned}
\tag{32}
$$

for the wave pattern in Fig. 3 and

$$
\begin{aligned}
&\rho_0^* = \rho_R^*\left(\frac{p_L^*}{p_R^*}\right)^{1/\gamma},\\
&u_0^* = u_L^*,\\
&p_0^* = p_L^*
\end{aligned}
\tag{33}
$$

for the other wave pattern.

Another possible way to solve the nonlinear equations across the solid contact is to rewrite them in terms of velocities, and iterate with respect to variables $u_L^*, u_R^*, \bar{u}_L^*, \bar{u}_R^*$. From the theoretical point of view there is no difference between these two approaches, as the system remains the same, but in practice the iterations in terms of pressures proved to be more robust for severe test problems with very low pressures or densities. Iteration in terms of velocities fail to compute such test cases, as there is no mechanism to control pressure positivity. All the results of this paper are therefore obtained using pressure iterations.

A useful observation concerning the number of iterations can be made from our numerical tests. It appears that 1-2 iterations are sufficient for convergence of Newton's method for all the test cases studied, and therefore our approximate Riemann solver is essentially a predictor–corrector scheme.

3.4. Wave speed estimates

Relations (22)–(25) for the intermediate HLLC states assume the estimates of the wave speeds $\bar{S}_L, \bar{S}_R, S_R$ and S_L, which must be known at each step of Newton's iteration. Several possible estimations for these velocities were proposed in [18]. For the Euler equations one choice is

$$
\begin{aligned}
&\bar{S}_L = \bar{u}_L - \bar{a}_L, \quad \bar{S}_R = \bar{u}_R + \bar{a}_R;\\
&S_L = u_L - a_L, \quad S_R = u_R + a_R.
\end{aligned}
$$

Another choice is to use pressure-based wave speed estimates

$$
\begin{aligned}
&\bar{S}_L = \bar{u}_L - \bar{a}_L\bar{q}_L, \quad \bar{S}_R = \bar{u}_R + \bar{a}_R\bar{q}_R,\\
&S_L = u_L - a_L q_L, \quad S_R = u_R + a_R q_R,
\end{aligned}
\tag{34}
$$

where the functions $\bar{q}_K$ and q_K take the following form for $K = L, R$:

$$
\bar{q}_K = \begin{cases} 1, & \text{if } \bar{p}_K^* \leqslant \bar{p}_K; \text{ (rarefaction)},\\ \left[1 + \frac{\bar{\gamma}+1}{2\bar{\gamma}}\left(\frac{\bar{p}_K^* + \bar{P}_0}{\bar{p}_K + \bar{P}_0} - 1\right)\right]^{\frac{1}{2}}, & \text{if } \bar{p}_K^* > \bar{p}_K, \text{ (shock wave)}, \end{cases}
\tag{35}
$$

$$
q_K = \begin{cases} 1, & \text{if } p_K^* \leqslant p_K; \text{ (rarefaction)},\\ \left[1 + \frac{\gamma+1}{2\gamma}\left(\frac{p_K^*}{p_K} - 1\right)\right]^{\frac{1}{2}}, & \text{if } p_K^* > p_K, \text{(shock wave)}, \end{cases}
\tag{36}
$$

where $a_K = \sqrt{\gamma p_K/\rho_K}, \bar{a}_K = \sqrt{\gamma(\bar{p}_K + \bar{P}_0)/\bar{\rho}_K}, K = L, R$ are the sound speeds for gas and solid phase, respectively.

There is a possibility of upgrading the wave speed estimates after each iteration if the scheme is used in iterative mode. The second variant is found to be more reliable and robust. We therefore use this method in all the computations presented in this paper.

The algorithm can be summarized as follows: we solve the nonlinear system of Eq. (30) (or (31), depending on the type of "subsonic" wave pattern) in terms of pressures $p_L^*, p_R^*, \bar{p}_L^*, \bar{p}_R^*$, using the expressions (26)–(29) for the densities and velocities present in the thin-layer equations, with any of the above described wave speed estimates. Having defined the solid and gas intermediate pressures, we recompute the intermediate velocities and densities according to (26)–(29) and (32) and (33).

4. Assessment of HLLC-type solver on local Riemann problems

In this section we assess the performance of the HLLC-type Riemann solver derived in the previous section on several test cases, comparing the intermediate states with those of the exact Riemann solver. We present results for six test problems shown in Tables 2–13. Tests 1 and 2 were taken from [9], Test 3 includes a sonic rarefaction, Test 4 is a severe test problem with a low-density flow, Test 5 assesses the resolution of stationary contact discontinuities and Test 6 includes very strong-shock waves.

The EOS parameters for the considered test problems are listed in Table 1. The solution values of the solid volume fraction, densities, velocities, pressures and gas densities, velocities and pressures obtained by the exact and approximate Riemann solvers are listed in Tables 2–13.

Table 1
EOS parameters.

	Test 1	Test 2	Test 3	Test 4	Test 5	Test 6
$\bar{\gamma}$	1.4	3.0	1.4	1.4	3.0	3.0
γ	1.4	1.35	1.4	1.4	1.4	1.4
$\bar{p}_0$	0.0	3400.0	0.0	0.0	10.0	100.0

Table 2
Test 1 (exact solution).

	Region L	Region $^*L$	Region ^{*0}	Region $^*R$	Region R
$\bar{\alpha}$	0.8	0.8	0.8	0.3	0.3
$\bar{\rho}$	1.0	0.9436	0.9436	1.0591	1.0
$\bar{u}$	0.0	0.0684	0.0684	0.0684	0.0
$\bar{p}$	1.0	0.9219	0.9219	1.0837	1.0
ρ	0.2	0.3266	0.6980	0.9058	1.0
u	0.0	−0.7683	−0.7683	−0.1159	0.0
p	0.3	0.6045	0.6045	0.8707	1.0

Table 3
Test 1 (approximate solution).

	Region L	Region $^*L$	Region ^{*0}	Region $^*R$	Region R
$\bar{\alpha}$	0.8	0.8	0.8	0.3	0.3
$\bar{\rho}$	1.0	0.9446	0.9446	1.0545	1.0
$\bar{u}$	0.0	0.0693	0.0693	0.0632	0.0
$\bar{p}$	1.0	0.9180	0.9180	1.0772	1.0
ρ	0.2	0.3257	0.7040	0.9115	1.0
u	0.0	−0.7631	−0.7631	−0.1149	0.0
p	0.3	0.6018	0.6018	0.8641	1.0

Table 4
Test 2 (exact solution).

	Region L	Region $^*L$	Region ^{*0}	Region $^*R$	Region R
$\bar{\alpha}$	0.2	0.2	0.9	0.9	0.9
$\bar{\rho}$	1900.0	2040.1092	1821.4053	1821.4053	1950.0
$\bar{u}$	0.0	−0.1716	−0.1716	−0.1716	0.0
$\bar{p}$	10.0	824.4354	185.6560	185.6560	1000.0
ρ	2.0	2.1093	1.6733	1.8554	1.0
u	0.0	−0.0761	0.7912	0.7912	0.0
p	3.0	3.2235	2.3580	2.3580	1.0

Table 5
Test 2 (approximate solution).

	Region L	Region $^*L$	Region ^{*0}	Region $^*R$	Region R
$\bar{\alpha}$	0.2	0.2	0.9	0.9	0.9
$\bar{\rho}$	1900.0	2030.2381	1834.8937	1834.8937	1950.0
$\bar{u}$	0.0	−0.1594	−0.1632	−0.1632	0.0
$\bar{p}$	10.0	762.8331	171.9396	171.9396	1000.0
ρ	2.0	2.0930	1.6298	1.8108	1.0
u	0.0	−0.0649	0.7558	0.7558	0.0
p	3.0	3.1898	2.2756	2.2756	1.0

Table 6
Test 3 (exact solution).

	Region L	Region $^*L$	Region ^{*0}	Region $^*R$	Region R
$\bar{\alpha}$	0.8	0.8	0.8	0.3	0.3
$\bar{\rho}$	1.0	0.5799	0.5799	0.3397	0.125
$\bar{u}$	0.75	1.3609	1.3609	1.3609	0.0
$\bar{p}$	1.0	0.4663	0.4663	0.4663	0.1
ρ	1.0	0.5799	0.3397	0.3397	0.125
u	0.75	1.3609	1.3609	1.3609	0.0
p	1.0	0.4663	0.4663	0.4662	0.1

Table 7
Test 3 (approximate solution).

	Region L	Region $^*L$	Region ^{*0}	Region $^*R$	Region R
$\bar{\alpha}$	0.8	0.8	0.8	0.3	0.3
$\bar{\rho}$	1.0	0.7389	0.7389	0.3542	0.125
$\bar{u}$	0.75	1.1680	1.1680	1.4487	0.0
$\bar{p}$	1.0	0.5054	0.5054	0.5054	0.1
ρ	1.0	0.7389	0.3542	0.3542	0.125
u	0.75	1.1680	1.1680	1.4487	0.0
p	1.0	0.5053	0.5054	0.5054	0.1

Table 8
Test 4 (exact solution).

	Region L	Region $^*L$	Region ^{*0}	Region $^*R$	Region R
$\bar{\alpha}$	0.8	0.8	0.5	0.5	0.5
$\bar{\rho}$	1.0	0.0219	0.0219	0.0219	1.0
$\bar{u}$	−2.0	0.0	0.0	0.0	2.0
$\bar{p}$	0.4	0.0019	0.0019	0.0019	0.4
ρ	1.0	0.0219	0.0219	0.0219	1.0
u	−2.0	0.0	0.0	0.0	2.0
p	0.4	0.0019	0.0019	0.0019	0.4

Table 9
Test 4 (approximate solution).

	Region L	Region $^*L$	Region ^{*0}	Region $^*R$	Region R
$\bar{\alpha}$	0.8	0.8	0.5	0.5	0.5
$\bar{\rho}$	1.0	0.2723	0.2723	0.2723	1.0
$\bar{u}$	−2.0	0.0	0.0	0.0	2.0
$\bar{p}$	0.4	10^{-6}	10^{-6}	10^{-6}	0.4
ρ	1.0	0.2723	0.2723	0.2723	1.0
u	−2.0	0.0	0.0	0.0	2.0
p	0.4	10^{-6}	10^{-6}	10^{-6}	0.4

Table 10
Test 5 (exact solution).

	Region L	Region $^*L$	Region ^{*0}	Region $^*R$	Region R
$\bar{\alpha}$	0.6	0.6	0.3	0.3	0.3
$\bar{\rho}$	1.4	1.4	1.0	1.0	1.0
$\bar{u}$	0.0	0.0	0.0	0.0	0.0
$\bar{p}$	2.0	2.0	3.0	3.0	3.0
ρ	1.4	1.4	1.4	1.0	1.0
u	0.0	0.0	0.0	0.0	0.0
p	1.0	1.0	1.0	1.0	1.0

Table 11
Test 5 (approximate solution).

	Region L	Region $^*L$	Region ^{*0}	Region $^*R$	Region R
$\bar{\alpha}$	0.6	0.6	0.3	0.3	0.3
$\bar{\rho}$	1.4	1.4	0.9999	0.9999	1.0
$\bar{u}$	0.0	0.0	0.0	0.0	0.0
$\bar{p}$	2.0	2.0	2.9999	2.9999	3.0
ρ	1.4	1.3999	1.4	1.0	1.0
u	0.0	0.0	0.0	0.0	0.0
p	1.0	0.9999	1.0	1.0	1.0

Table 12
Test 6 (exact solution).

	Region L	Region $^*L$	Region ^{*0}	Region $^*R$	Region R
$\bar{\alpha}$	0.7	0.7	0.2	0.2	0.2
$\bar{\rho}$	1.0	0.7687	1.6087	1.6087	1.0
$\bar{u}$	−19.5975	−6.3085	−6.3085	−6.3085	−19.5975
$\bar{p}$	1000.0	399.5878	466.7257	466.7257	0.01
ρ	1.0	0.4684	0.5030	5.9991	1.0
u	−19.5975	6.7332	−1.7541	−1.7541	−19.5975
p	1000.0	345.8279	382.0858	382.0858	0.01

Table 13
Test 6 (approximate solution).

	Region L	Region $^*L$	Region ^{*0}	Region $^*R$	Region R
$\bar{\alpha}$	0.7	0.7	0.2	0.2	0.2
$\bar{\rho}$	1.0	0.8372	1.5648	1.5648	1.0
$\bar{u}$	0.0	−8.4297	−7.7409	−7.7409	0.0
$\bar{p}$	1000.0	358.4630	389.4630	389.4630	0.01
ρ	1.0	0.6778	0.6978	5.9990	1.0
u	0.0	−1.8135	−2.5577	−2.5577	0.0
p	1000.0	334.5839	348.4473	348.4473	0.01

Results indicate that our approximate Riemann solver produces accurate intermediate states (see Fig. 1) for most test cases. Inaccuracies appear on very severe test problems, including low-pressure flow or very strong shocks, in these situations the approximate intermediate states can differ significantly from the exact ones. However, such inaccuracy in the states does not deteriorate the quality of the numerical fluxes derived from our Riemann solver when implemented in numerical schemes.

The main purpose of this paper is the development of the HLLC-type approximate Riemann solver to be used in numerical methods. This is done in Sections 5 and 6.

5. HLLC-type Riemann solver in the finite volume and discontinuous Galerkin finite element methods

In this section we derive the numerical flux based on the approximate Riemann solver and use it as a building block for the first-order finite volume Godunov scheme described in [9] and a second-order discontinuous Galerkin scheme [23] based on the formulation of van der Vegt et al. [24]. In Section 6 we apply the Riemann solver to a path-conservative scheme.

5.1. Numerical flux

Having defined the intermediate states by the approximate Riemann solver we can use them to construct the numerical flux for the conservative part of the system (1). Consider again Figs. 2 and 3. The $x-t$ plane for the solid phase is separated by the wave families into four regions of constant states $\bar{\mathbf{U}}$, and we thus need to identify the flux vector in each of these regions. For the gas phase, there are five regions of constant states $\mathbf{U}$, and we also need to find the numerical flux in these regions. The flux for the solid phase (here $\bar{S}_M = \bar{u}_L^* = \bar{u}_R^*$) is

$$\bar{\mathscr{G}}(\bar{\mathbf{U}}_L, \bar{\mathbf{U}}_R) = \begin{cases} \bar{\mathbf{G}}_L, & 0 \leqslant \bar{S}_L; \\ \bar{\mathbf{G}}_L^* = \bar{\mathbf{G}}_L + \bar{S}_L(\bar{\mathbf{U}}_L^* - \bar{\mathbf{U}}_L), & \bar{S}_L \leqslant 0 \leqslant \bar{S}_M; \\ \bar{\mathbf{G}}_R^* = \bar{\mathbf{G}}_R + \bar{S}_R(\bar{\mathbf{U}}_R^* - \bar{\mathbf{U}}_R), & \bar{S}_M \leqslant 0 \leqslant \bar{S}_R; \\ \bar{\mathbf{G}}_R, & \bar{S}_R \leqslant 0, \end{cases} \tag{37}$$

where $\bar{\mathbf{G}}_L = \bar{\mathbf{G}}(\bar{\mathbf{U}}_L), \bar{\mathbf{G}}_R = \bar{\mathbf{G}}(\bar{\mathbf{U}}_R)$.

For the gas phase, when the solid-phase contact lies to the left of gas-phase contact (Fig. 3), we have the following expressions ($S_M = u_0^* = u_R^*$):

$$\mathscr{G}(\mathbf{U}_L, \mathbf{U}_R) = \begin{cases} \mathbf{G}_L, & 0 \leqslant S_L; \\ \mathbf{G}_L^* = \mathbf{G}_L + S_L(\mathbf{U}_L^* - \mathbf{U}_L), & S_L \leqslant 0 \leqslant \bar{S}_M; \\ \mathbf{G}_0^* = \mathbf{G}_R + S_R(\mathbf{U}_R^* - \mathbf{U}_R) + S_M(\mathbf{U}_0^* - \mathbf{U}_R^*), & \bar{S}_M \leqslant 0 \leqslant S_M; \\ \mathbf{G}_R^* = \mathbf{G}_R + S_R(\mathbf{U}_R^* - \mathbf{U}_R), & S_M \leqslant 0 \leqslant S_R; \\ \mathbf{G}_R, & S_R \leqslant 0. \end{cases} \tag{38}$$

If the solid-phase contact is situated to the right of the gas-phase contact, we will have similar expressions for the flux ($S_M = u_0^* = u_L^*$):

$$\mathscr{G}(\mathbf{U}_L, \mathbf{U}_R) = \begin{cases} \mathbf{G}_L, & 0 \leqslant S_L; \\ \mathbf{G}_L^* = \mathbf{G}_L + S_L(\mathbf{U}_L^* - \mathbf{U}_L), & S_L \leqslant 0 \leqslant S_M; \\ \mathbf{G}_0^* = \mathbf{G}_L + S_L(\mathbf{U}_L^* - \mathbf{U}_L) + S_M(\mathbf{U}_0^* - \mathbf{U}_L^*), & S_M \leqslant 0 \leqslant \bar{S}_M; \\ \mathbf{G}_R^* = \mathbf{G}_R + S_R(\mathbf{U}_R^* - \mathbf{U}_R), & \bar{S}_M \leqslant 0 \leqslant S_R; \\ \mathbf{G}_R, & S_R \leqslant 0, \end{cases} \tag{39}$$

where $\mathbf{G}_L = \mathbf{G}(\mathbf{U}_L), \mathbf{G}_R = \mathbf{G}(\mathbf{U}_R)$.

The resulting flux for the whole system is then constructed from $\bar{\mathscr{G}}$ and $\mathscr{G}$ as follows:

$$\widehat{\mathbf{F}}(\mathbf{Q}_L, \mathbf{Q}_R) = \begin{bmatrix} 0 \\ \bar{\mathscr{G}} \\ \mathscr{G} \end{bmatrix}.$$

In (37)–(39) we assume the HLLC definitions for the states ($K = L, R$):

$$\bar{\mathbf{U}}_K^* = \bar{\alpha}_K \bar{\rho}_K \left(\frac{\bar{S}_K - \bar{u}_K}{\bar{S}_K - \bar{S}_M} \right) \begin{bmatrix} 1 \\ \bar{S}_M \\ \bar{E}_K + (\bar{S}_M - \bar{u}_K)\left(\bar{S}_M + \frac{\bar{p}_K}{\bar{\rho}_K(\bar{S}_K - \bar{u}_K)} \right) \end{bmatrix},$$

$$\mathbf{U}_K^* = \alpha_K \rho_K \left(\frac{S_K - u_K}{S_K - S_M} \right) \begin{bmatrix} 1 \\ S_M \\ E_K + (S_M - u_K)\left(S_M + \frac{p_K}{\rho_K(S_K - u_K)} \right) \end{bmatrix},$$

$$\mathbf{U}_0^* = \begin{bmatrix} \alpha_0 \rho_0^* \\ \alpha_0 \rho_0^* u_0^* \\ \alpha_0 \rho_0^* E_0^* \end{bmatrix},$$

where for the wave configuration presented in Fig. 3

$$
\begin{aligned}
&\alpha_0 = \alpha_R,\\
&\rho_0^* = \rho_L^*\left(\frac{p_R^*}{p_L^*}\right)^{1/\gamma},\\
&u_0^* = u_R^*,\\
&p_0^* = p_R^*,\\
&E_0^* = \frac{p_0^*}{(\gamma-1)\rho_0^*} + \frac{1}{2}u_0^*
\end{aligned}
$$

and for the other wave configuration

$$
\begin{aligned}
&\alpha_0 = \alpha_L,\\
&\rho_0^* = \rho_R^*\left(\frac{p_L^*}{p_R^*}\right)^{1/\gamma},\\
&u_0^* = u_L^*,\\
&p_0^* = p_L^*,\\
&E_0^* = \frac{p_0^*}{(\gamma-1)\rho_0^*} + \frac{1}{2}u_0^*.
\end{aligned}
$$

5.2. Finite volume method

Assume a finite-volume mesh with volumes $[x_{j-\frac{1}{2}}, x_{j+\frac{1}{2}}] \times [t_n, t_{n+1}]$, cell boundaries $x_{j+\frac{1}{2}}$, cell spacing $\Delta x_j = x_{j+\frac{1}{2}} - x_{j-\frac{1}{2}}$, cell centre $x_j = \frac{1}{2}(x_{j-\frac{1}{2}} + x_{j+\frac{1}{2}})$ and time step $\Delta t_n = t_{n+1} - t_n$. We define the cell average

$$
\mathbf{Q}_j^n = \frac{1}{\Delta x_j}\int_{x_{j-\frac{1}{2}}}^{x_{j+\frac{1}{2}}} \mathbf{Q}(x, t_n)dx
$$

and integrate the equations over the volume $\Omega_j^n = [x_{j-\frac{1}{2}}, x_{j+\frac{1}{2}}] \times [t_n, t_{n+1}]$ to obtain the exact relation

$$
\mathbf{Q}_j^{n+1} = \mathbf{Q}_j^n - \frac{\Delta t^n}{\Delta x_j}\left(\mathbf{F}_{j+\frac{1}{2}^n} - \mathbf{F}_{j-\frac{1}{2}^n}\right) - \frac{1}{\Delta x_j}\int\int_{\Omega_j^n} \mathbf{T}(\mathbf{Q})\partial_x\bar{\alpha}\,dx\,dt, \tag{40}
$$

where

$$
\mathbf{F}_{j-\frac{1}{2}}^n = \widehat{\mathbf{F}}(\mathbf{Q}_{j-1}^n, \mathbf{Q}_j^n) = \frac{1}{\Delta t_n}\int_{t_n}^{t_{n+1}} \mathbf{F}\left(\mathbf{Q}\left(x_{j-\frac{1}{2}}, t\right)\right)dt.
$$

We use the same approach as in [9] to approximate the integrals of nonconservative terms in (40). We first apply our Riemann solver to define all the intermediate states of the solution, after that we use the following approximation of the term $\frac{1}{\Delta t_n}\int\int_{\Omega_j^n} \mathbf{T}(\mathbf{Q})\partial_x\bar{\alpha}\,dx\,dt$ (compare with (16)):

$$
\widehat{\mathbf{T}}(\mathbf{Q}_L, \mathbf{Q}_R) = \begin{bmatrix}
\bar{S}_M(\bar{\alpha}_R - \bar{\alpha}_L)\\
0\\
-(\bar{p}_R^*\bar{\alpha}_R - \bar{p}_L^*\bar{\alpha}_L)\\
-\bar{S}_M(\bar{p}_R^*\bar{\alpha}_R - \bar{p}_L^*\bar{\alpha}_L)\\
0\\
\bar{p}_R^*\bar{\alpha}_R - \bar{p}_L^*\bar{\alpha}_L\\
\bar{S}_M(\bar{p}_R^*\bar{\alpha}_R - \bar{p}_L^*\bar{\alpha}_L)
\end{bmatrix}.
$$

The resulting finite-volume Godunov scheme for Eq. (1) takes the form

$$
\mathbf{Q}_j^{n+1} = \mathbf{Q}_j^n - \frac{\Delta t^n}{\Delta x_j}\left(\mathbf{H}_{j+\frac{1}{2}}^- - \mathbf{H}_{j-\frac{1}{2}}^+\right),
$$

where $\mathbf{H}_{j-\frac{1}{2}}^-$ and $\mathbf{H}_{j-\frac{1}{2}}^+$ satisfy

$$\mathbf{H}^{-}_{j-\frac{1}{2}} = \begin{cases} \widehat{\mathbf{F}}(\mathbf{Q}^n_{j-1}, \mathbf{Q}^n_j) + \widehat{\mathbf{T}}(\mathbf{Q}^n_{j-1}, \mathbf{Q}^n_j), & \text{if } \bar{S}^n_{M,j-\frac{1}{2}} \leqslant 0, \\ \widehat{\mathbf{F}}(\mathbf{Q}^n_{j-1}, \mathbf{Q}^n_j), & \text{if } \bar{S}^n_{M,j-\frac{1}{2}} > 0, \end{cases}$$

$$\mathbf{H}^{+}_{j-\frac{1}{2}} = \begin{cases} \widehat{\mathbf{F}}(\mathbf{Q}^n_{j-1}, \mathbf{Q}^n_j), & \text{if } \bar{S}^n_{M,j-\frac{1}{2}} \leqslant 0, \\ \widehat{\mathbf{F}}(\mathbf{Q}^n_{j-1}, \mathbf{Q}^n_j) - \widehat{\mathbf{T}}(\mathbf{Q}^n_{j-1}, \mathbf{Q}^n_j), & \text{if } \bar{S}^n_{M,j-\frac{1}{2}} > 0. \end{cases}$$

5.3. Discontinuous Galerkin finite element method

Consider Eq. (1) in the one-dimensional computational domain $[0,1]$. We seek the approximate solution $\mathbf{Q}_h(x,t)$ of (1) as a piecewise-polynomial function in space, i.e. the approximate solution $\mathbf{Q}^j_h$ within each computational cell $I_j = [x_{j-\frac{1}{2}}, x_{j+\frac{1}{2}}]$ is a polynomial of degree k. Such solution can be represented as an expansion over basis functions

$$\mathbf{Q}^j_h(x,t) = \sum_{l=0}^{k} \mathbf{Q}^l_j(t)\varphi_l(x),$$

$$\varphi_l(x) = P_l\left(\frac{2(x-x_j)}{\Delta x_j}\right), \quad \Delta x_j = x_{j+\frac{1}{2}} - x_{j-\frac{1}{2}}, \quad x_j = \frac{x_{j+\frac{1}{2}} + x_{j-\frac{1}{2}}}{2},$$

where P_l is a Legendre polynomial of order l. In this paper we restrict ourselves to piecewise-linear approximations. Assume there exists a function such that

$$\widetilde{\mathbf{F}}(\mathbf{Q}) = \frac{\partial \widetilde{\mathbf{T}}(\mathbf{Q})}{\partial \mathbf{Q}},$$

$$\widetilde{\mathbf{T}}(\mathbf{Q}) = [\mathbf{T}(\mathbf{Q}), \ldots, \mathbf{0}],$$

where $\mathbf{Q}$ and $\mathbf{T}$ are given in (1). Then, we can rewrite the governing equations in conservative form, with $\mathbf{H} = \mathbf{F} + \widetilde{\mathbf{F}}$:

$$\partial_t \mathbf{Q} + \partial_x \mathbf{H}(\mathbf{Q}) = \mathbf{0}. \tag{41}$$

We integrate the governing equations multiplied by basis function φ_i over each computational cell. To obtain a weak solution of (41):

$$\int_{I_j} \partial_t \mathbf{Q}\varphi_i(x)dx - \int_{I_j} \mathbf{H}(\mathbf{Q})\partial_x\varphi_i(x)dx + (\mathbf{H}(\mathbf{Q})\varphi_i(x))|^{x_{j+\frac{1}{2}}}_{x_{j-\frac{1}{2}}} = 0.$$

Using the theory of Dal Maso et al. [25] the following weak formulation can be obtained:

$$\int_{I_j} \partial_t \mathbf{Q}\varphi_i(x)dx - \int_{I_j} \mathbf{F}(\mathbf{Q})\partial_x\varphi_i(x)dx + (\mathbf{H}(\mathbf{Q})\varphi_i(x))|^{x_{j+\frac{1}{2}}}_{x_{j-\frac{1}{2}}} = -\int_{I_j} \mathbf{T}(\mathbf{Q})\partial_x\tilde{\alpha}\varphi_i(x)dx - \left(\frac{1}{2}\varphi_i(x)\int_0^1 \mathbf{T}(\bar{\varphi}(s;\mathbf{Q}_L,\mathbf{Q}_R))\frac{\partial\bar{\varphi}}{\partial s}d\tau\right)\Bigg|^{x_{j+\frac{1}{2}}}_{x_{j-\frac{1}{2}}}, \tag{42}$$

where a path $\bar{\varphi}(s;\mathbf{Q}_L,\mathbf{Q}_R)$ is introduced, satisfying the properties

$$\bar{\varphi} : [0,1] \times \mathbf{R}^n \times \mathbf{R}^n \to \mathbf{R}^n,$$

$$\bar{\varphi}(0,\mathbf{Q}_L,\mathbf{Q}_R) = \mathbf{Q}_L, \bar{\varphi}(1,\mathbf{Q}_L,\mathbf{Q}_R) = \mathbf{Q}_R.$$

We use a linear path in our computations, namely

$$\bar{\varphi}(s,\mathbf{Q}_L,\mathbf{Q}_R) = \mathbf{Q}_L + s(\mathbf{Q}_R - \mathbf{Q}_L), \quad s \in [0,1].$$

Then we take into account the piecewise-linear approximation of the solution. That is, the solution inside the jth computational cell is represented as a linear combination

$$\mathbf{Q}^j_h = \mathbf{Q}^j_0(t)\varphi^j_0(x) + \mathbf{Q}^j_1(t)\varphi^j_1(x), \tag{43}$$

where

$$\varphi^j_0(x) = 1, \quad \varphi^j_1(x) = \frac{2(x-x_j)}{\Delta x_j}.$$

Substituting (43) to (42), we obtain the following ODE system for the degrees of freedom in the basis expansion for jth computational cell:

$$\frac{d\mathbf{Q}_0^j(t)}{dt} = \frac{1}{\Delta x_j}\left[\mathbf{P}_{j-\frac{1}{2}}(Q_h) - \mathbf{P}_{j+\frac{1}{2}}(\mathbf{Q}_h) - \int_{I_j}\mathbf{T}(\mathbf{Q}_h)\partial_x\bar{\alpha}dx - \frac{1}{2}\int_0^1 \mathbf{T}\left(\bar{\varphi}(s;\bar{\mathbf{Q}}_{j+\frac{1}{2}})\right)\frac{\partial\bar{\varphi}}{\partial s}d\tau + \frac{1}{2}\int_0^1 \mathbf{T}\left(\bar{\varphi}(s;\bar{\mathbf{Q}}_{j-\frac{1}{2}})\right)\frac{\partial\bar{\varphi}}{\partial s}d\tau\right], \tag{44}$$

$$\frac{d\mathbf{Q}_1^j(t)}{dt} = \frac{3}{\Delta x_j}\left[\int_{I_j}\mathbf{F}(\mathbf{Q}_h)\frac{2}{\Delta x_j}dx - \mathbf{P}_{j-\frac{1}{2}}(\mathbf{Q}_h) - \mathbf{P}_{j+\frac{1}{2}}(\mathbf{Q}_h) - \int_{I_j}\mathbf{T}(\mathbf{Q}_h)\partial_x\bar{\alpha}\frac{2(x-x_j)}{\Delta x_j}dx - \frac{1}{2}\int_0^1 \mathbf{T}\left(\bar{\varphi}(s;\bar{\mathbf{Q}}_{j+\frac{1}{2}})\right)\frac{\partial\bar{\varphi}}{\partial s}d\tau - \frac{1}{2}\int_0^1 \mathbf{T}\left(\bar{\varphi}(s;\bar{\mathbf{Q}}_{j-\frac{1}{2}})\right)\frac{\partial\bar{\varphi}}{\partial s}d\tau\right], \tag{45}$$

where $\bar{\mathbf{Q}}_{j+\frac{1}{2}} = \left[\mathbf{Q}_L^{j+\frac{1}{2}}, \mathbf{Q}_R^{j+\frac{1}{2}}\right]$ are boundary extrapolated values of the approximate solution in the jth and $(j+1)$st cells at the cell interface $j+\frac{1}{2}$.

In (44) and (45) $\mathbf{P}_{j+\frac{1}{2}}(\mathbf{Q}_h)$ denotes the nonconservative numerical flux through the cell interface. This flux depends on the values of the numerical solution on both sides of the cell interface $\bar{\mathbf{Q}}_{j+\frac{1}{2}}$. This numerical flux is an approximation of the "conservative" intercell flux $\mathbf{H}(\mathbf{Q})$, however, it actually consists of a conservative and nonconservative parts. The general construction of such flux was derived in [24] and can be directly applied to the nonconservative system describing two-phase flows.

We use the Riemann solver of this paper and the numerical flux derived in Section 5.1 to approximate the conservative part of $\mathbf{P}$ and add the term corresponding to the nonconservative part.

The resulting nonconservative flux $\mathbf{P}$ can then be approximated as

$$\mathbf{P}|_{x_{j+\frac{1}{2}}} = \widehat{\mathbf{F}}(\mathbf{Q}_L, \mathbf{Q}_R) - \frac{1}{2}\int_0^1 \mathbf{T}(\bar{\varphi}(s;\mathbf{Q}_L,\mathbf{Q}_R))\frac{\partial\bar{\varphi}}{\partial s}\,d\tau, \tag{46}$$

where $\mathbf{Q}_L$ and $\mathbf{Q}_R$ are the states to the left and right of the cell interface $x_{j+\frac{1}{2}}$, respectively, and $\widehat{\mathbf{F}}$ is the numerical flux based on our Riemann solver.

Another important stage in the construction of the numerical scheme is the approximation of the volume fraction derivative $\partial_x\bar{\alpha}$. As the numerical solution is piecewise linear, one possible way is to use directly the piecewise constant derivative of the approximate solution. However, this approach does not give satisfactory results, as the possible volume fraction jump across the cell interface is not taken into account.

In this paper we use a different formulation. We introduce additional variables representing the volume fraction derivative, so that it becomes an independent variable and we can find a piecewise-linear approximation of the volume fraction gradient:

$$\partial_x\bar{\alpha} = \mathbf{V}. \tag{47}$$

We use the same approach to find the approximation of the $\mathbf{V}$ variable, namely, we represent $\mathbf{V}$ as a linear function inside the jth computational cell:

$$\mathbf{V}_h^j = \mathbf{V}_0^j(t)\varphi_0^j(x) + \mathbf{V}_1^j(t)\varphi_1^j(x) \tag{48}$$

multiply Eq. (47) by basis functions φ_0 and φ_1, use expression (48) for the volume fraction derivative and integrate over I_j. Finally we obtain the following definitions for the degrees of freedom of $\mathbf{V}_h^j$:

$$\mathbf{V}_0^j(t) = \frac{1}{\Delta x_j}\left[\bar{\alpha}_{j+\frac{1}{2}} - \bar{\alpha}_{j-\frac{1}{2}}\right],$$

$$\mathbf{V}_1^j(t) = \frac{3}{\Delta x_j}\left[\bar{\alpha}_{j+\frac{1}{2}} + \bar{\alpha}_{j-\frac{1}{2}} - \int_{I_j}\bar{\alpha}_h^j(x)\frac{2}{\Delta x_j}dx\right],$$

where $\bar{\alpha}_h^j(x)$ is a linear approximation of $\bar{\alpha}(x)$ on I_j and $\bar{\alpha}_{j\pm\frac{1}{2}}$ are the estimations of the solid volume fraction on cell interfaces. There are several ways to find these estimates, one of them is to take the average value of the volume fractions to the left and right sides of the cell interface. This approach is simple, but on solutions with large volume fraction jumps it can produce spurious oscillations. We thus use a different approach based on a partial analysis of the Riemann problem solution for (1), namely, we assume

$$\bar{\alpha}_{j\pm\frac{1}{2}} = \bar{\alpha}_L, \quad \text{if } \bar{S}_M \geqslant 0,$$

$$\bar{\alpha}_{j\pm\frac{1}{2}} = \bar{\alpha}_R, \quad \text{if } \bar{S}_M < 0,$$

where $\bar{\alpha}_L$ and $\bar{\alpha}_R$ are the left and right initial volume fractions of the Riemann problem and $\bar{S}_M$ is the speed of the solid contact (see Fig. 1).

Having approximated the volume fraction derivative, we need to select the appropriate quadrature rule for the cell integration. In our computations we have used different Gauss–Lobatto quadratures for nonconservative terms, which lead to approximately the same results beginning with the five-point rule. For the integrals of the conservative terms we use the three-point Gauss quadrature.

We use the explicit two-stage TVD Runge–Kutta scheme for the solution of the system of ODE (44) and (45). On each intermediate step of the Runge–Kutta procedure we apply a slope limiter similar to the one described in [23]. The limiting is performed in characteristic variables.

6. An HLLC-based path-conservative method

Conservative and nonconservative systems can all be written in the quasilinear (nonconservative) form

$$\partial_t \mathbf{Q} + \mathbf{A}(\mathbf{Q})\partial_x \mathbf{Q} = \mathbf{S}(\mathbf{Q}), \tag{49}$$

where $\mathbf{Q}$ is assumed to be the vector of physically conserved variables. In the conservative case $\mathbf{A}(\mathbf{Q})$ is the Jacobian matrix of a flux function $\mathbf{F}(\mathbf{Q})$, that is $\mathbf{A}(\mathbf{Q}) = \partial \mathbf{F}(\mathbf{Q})/\partial \mathbf{Q}$. In the nonconservative case such flux function is not available. A prominent example of a nonconservative hyperbolic system are the Baer–Nunziato equations, which are the equations of concern in this paper. In this section, after a brief introduction, we describe an upwind path-conservative scheme to solve numerically equations of the type (49); we also implement the new HLLC Riemann solver proposed in this paper in such numerical scheme.

6.1. Nonconservative systems and path-conservative methods

The difficulty in dealing with hyperbolic equations with nonconservative products, such as in (49), arises when solutions are discontinuous. Then we cannot apply the usual Rankine–Hugoniot jump condition to (49) to define shocks, as there is no flux function $\mathbf{F}(\mathbf{Q})$. Mathematically, equations of this type have been studied by Volpert [26] and many others, since then. More recently, Dal Maso and collaborators [25] have put forward a mathematical theory that allows the definition of weak solutions of nonconservative hyperbolic systems. A key ingredient of the theory is the definition of paths φ in phase space with the properties described in the previous section

$$\varphi : [0,1] \times \mathbf{R}^n \times \mathbf{R}^n \to \mathbf{R}^n.$$

An obvious and useful example of a path is the *canonical path*

$$\varphi(s, \mathbf{Q}_L, \mathbf{Q}_R) = \mathbf{Q}_L + s(\mathbf{Q}_R - \mathbf{Q}_L), \quad s \in [0,1]. \tag{50}$$

A shock solution of speed S of the form

$$\mathbf{Q}(x,t) = \begin{cases} \mathbf{Q}_L, & \text{if } x/t < S; \\ \mathbf{Q}_R, & \text{if } x/t > S \end{cases}$$

is required to satisfy *Generalised Rankine–Hugoniot* conditions

$$\int_0^1 S \frac{\partial}{\partial s} \varphi(s, \mathbf{Q}_L, \mathbf{Q}_R) ds = \int_0^1 \mathbf{A}(\varphi(s, \mathbf{Q}_L, \mathbf{Q}_R)) \frac{\partial}{\partial s} \varphi(s, \mathbf{Q}_L, \mathbf{Q}_R) ds. \tag{51}$$

Note that if the path (50) is used in (51) we obtain

$$S(\mathbf{Q}_R - \mathbf{Q}_L) = \left(\int_0^1 \mathbf{A}(\mathbf{Q}_L + s(\mathbf{Q}_R - \mathbf{Q}_L)) ds \right) (\mathbf{Q}_R - \mathbf{Q}_L).$$

Numerical methods to solve equations in nonconservative form can then be constructed following this mathematical theory of Dal Maso et al. [25]. The first reported attempt is due to Toumi [27]. Then Parés and collaborators [10,28] developed further this idea and introduced the concept of path-conservative schemes defined as

$$\mathbf{Q}_j^{n+1} = \mathbf{Q}_j^n - \frac{\Delta t}{\Delta x} \left[\mathbf{D}^+_{j-\frac{1}{2}} + \mathbf{D}^-_{j+\frac{1}{2}} \right], \tag{52}$$

where $\mathbf{D}^-_{j+\frac{1}{2}}$ and $\mathbf{D}^+_{j+\frac{1}{2}}$ satisfy

$$\mathbf{D}^-_{j+\frac{1}{2}}(\mathbf{Q}, \mathbf{Q}) = \mathbf{0}, \mathbf{D}^+_{j+\frac{1}{2}}(\mathbf{Q}, \mathbf{Q}) = \mathbf{0}$$

and

$$\mathbf{D}^-_{j+\frac{1}{2}} + \mathbf{D}^+_{j+\frac{1}{2}} = \int_0^1 \mathbf{A}\left(\varphi(s, \mathbf{Q}_j^n, \mathbf{Q}_{j+1}^n) \right) \frac{\partial}{\partial s} \varphi(s, \mathbf{Q}_j^n, \mathbf{Q}_{j+1}^n) \, ds.$$

Upwind path-conservative schemes have been constructed by resorting to the Roe ideas for conservative methods. To this end a Roe-type matrix $\widehat{\mathbf{A}}$ is defined as that possessing the usual three properties of Roe's method for conservative systems, namely hyperbolicity, consistency and conservation. The first two properties are obvious and the third one takes the form

$$\widehat{\mathbf{A}}(\mathbf{Q}_{j+1}^n - \mathbf{Q}_j^n) = \int_0^1 \mathbf{A}\left(\varphi(s, \mathbf{Q}_j^n, \mathbf{Q}_{j+1}^n) \right) \frac{\partial}{\partial s} \varphi(s, \mathbf{Q}_j^n, \mathbf{Q}_{j+1}^n) \, ds.$$

Given a Roe linearisation $\widehat{\mathbf{A}}$ one can define a path-conservative scheme of the form (52), where

Table 14
EOS parameters, initial discontinuity position.

	Test 1	Test 2	Test 3	Test 4	Test 5	Test 6
$\bar{\gamma}$	1.4	3.0	1.4	1.4	3.0	3.0
γ	1.4	1.35	1.4	1.4	1.4	1.4
$\bar{P}_0$	0.0	3400.0	0.0	0.0	10.0	100.0
x_0	0.5	0.5	0.5	0.5	0.5	0.8

Table 15
Initial data (solid phase).

Test	$\bar{\alpha}_L$	$\bar{\rho}_L$	$\bar{u}_L$	$\bar{p}_L$	$\bar{\alpha}_R$	$\bar{\rho}_R$	$\bar{u}_R$	$\bar{p}_R$
1	0.8	1.0	0.0	1.0	0.3	1.0	0.0	1.0
2	0.2	1900.0	0.0	10.0	0.9	1950.0	0.0	1000.0
3	0.8	1.0	0.75	1.0	0.3	0.125	0.0	0.1
4	0.8	1.0	−2.0	0.4	0.5	1.0	2.0	0.4
5	0.6	1.4	0.0	2.0	0.3	1.0	0.0	3.0
6	0.7	1.0	−19.5975	1000.0	0.2	1.0	−19.5975	0.01

Table 16
Initial data (gas phase).

Test	α_L	ρ_L	u_L	p_L	α_R	ρ_R	u_R	p_R
1	0.2	0.2	0.0	0.3	0.7	1.0	0.0	1.0
2	0.8	2.0	0.0	3.0	0.1	1.0	0.0	1.0
3	0.2	1.0	0.75	1.0	0.7	0.125	0.0	0.1
4	0.2	1.0	−2.0	0.4	0.5	1.0	2.0	0.4
5	0.4	1.4	0.0	1.0	0.7	1.0	0.0	1.0
6	0.3	1.0	−19.5975	1000.0	0.8	1.0	−19.5975	0.01

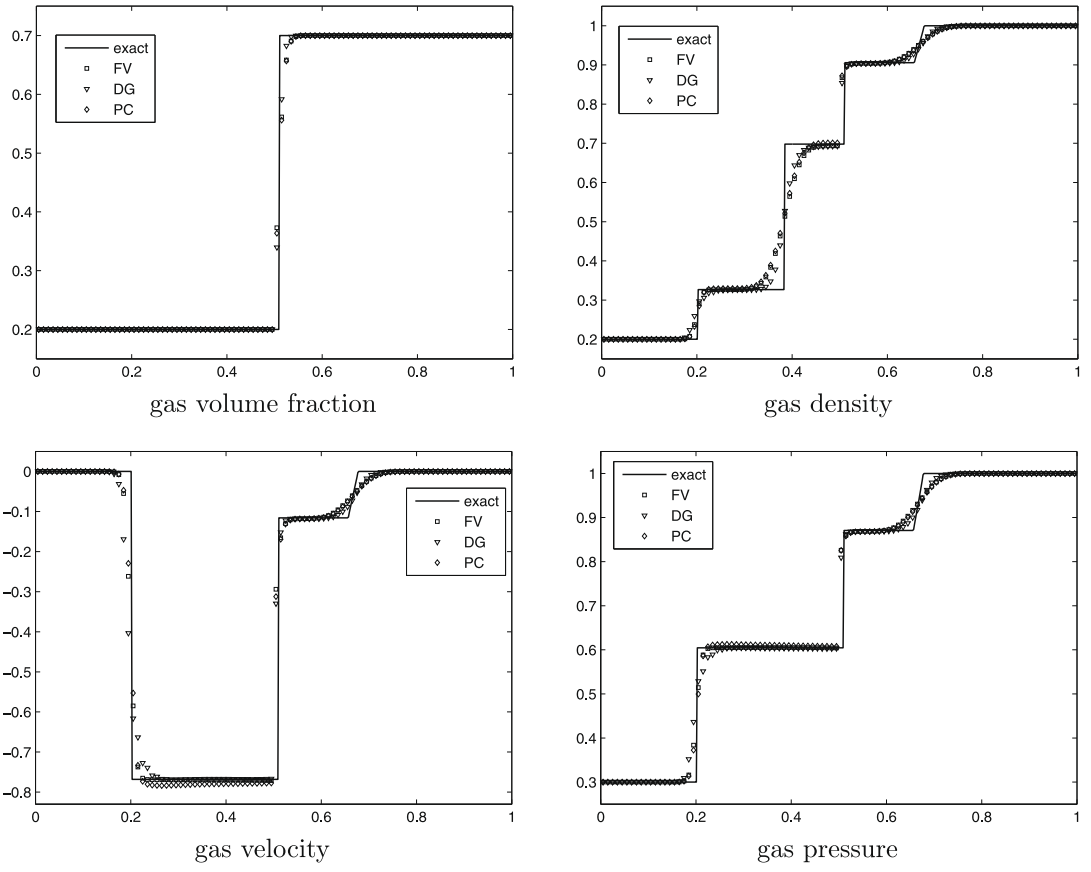

Fig. 4(a). Test 1. Results for the gas phase: computed (symbol) and exact solution (line) at time $t = 0.15$.

$$\mathbf{D}^-_{j+\frac{1}{2}} = \widehat{\mathbf{A}}^-_{j+\frac{1}{2}}(\mathbf{Q}^n_{j+1} - \mathbf{Q}^n_j), \mathbf{D}^+_{j+\frac{1}{2}} = \widehat{\mathbf{A}}^+_{j+\frac{1}{2}}(\mathbf{Q}^n_{j+1} - \mathbf{Q}^n_j),$$

with

$$\widehat{\mathbf{A}}^-_{j+\frac{1}{2}} = \mathbf{R}_{j+\frac{1}{2}}\Lambda^-_{j+\frac{1}{2}}\mathbf{R}^{-1}_{j+\frac{1}{2}}, \widehat{\mathbf{A}}^+_{j+\frac{1}{2}} = \mathbf{R}_{j+\frac{1}{2}}\Lambda^+_{j+\frac{1}{2}}\mathbf{R}^{-1}_{j+\frac{1}{2}}.$$

Here $\Lambda^-_{j+\frac{1}{2}}$ is the diagonal matrix of non-positive eigenvalues and $\Lambda^+_{j+\frac{1}{2}}$ is the diagonal matrix of non-negative eigenvalues, $\mathbf{R}_{j+\frac{1}{2}}$ is the matrix of right eigenvectors at the interface.

6.2. HLLC-based scheme

In this paper we construct an alternative upwind path-conservative method following the ideas of Muñoz and Parés [28]. Assume $\mathbf{Q}_{j+\frac{1}{2}}(x/t)$ is the solution of the Riemann problem

$$\begin{aligned} &\partial_t \mathbf{Q} + \mathbf{A}(\mathbf{Q})\partial_x \mathbf{Q} = \mathbf{0}, \\ &\mathbf{Q}(x,0) = \begin{cases} \mathbf{Q}^n_j, & \text{if } x < 0; \\ \mathbf{Q}^n_{j+1}, & \text{if } x > 0. \end{cases} \end{aligned} \tag{53}$$

We denote by $\mathbf{Q}_{j+\frac{1}{2}}(0)$ the corresponding Godunov state. Then a path-conservative scheme of the type (52) can be constructed by defining $\mathbf{D}^-_{j+\frac{1}{2}}$ and $\mathbf{D}^+_{j+\frac{1}{2}}$ as follows

$$\mathbf{D}^-_{j+\frac{1}{2}} = \int_0^1 \mathbf{A}\left(\varphi\left(s, \mathbf{Q}^n_j, \mathbf{Q}_{j+\frac{1}{2}}(0)\right)\right)\frac{\partial}{\partial s}\varphi\left(s, \mathbf{Q}^n_j, \mathbf{Q}_{j+\frac{1}{2}}(0)\right)ds \tag{54}$$

and

$$\mathbf{D}^+_{j+\frac{1}{2}} = \int_0^1 \mathbf{A}\left(\varphi\left(s, \mathbf{Q}_{j+\frac{1}{2}}(0), \mathbf{Q}^n_{j+1}\right)\right)\frac{\partial}{\partial s}\varphi\left(s, \mathbf{Q}_{j+\frac{1}{2}}(0), \mathbf{Q}^n_{j+1}\right)ds. \tag{55}$$

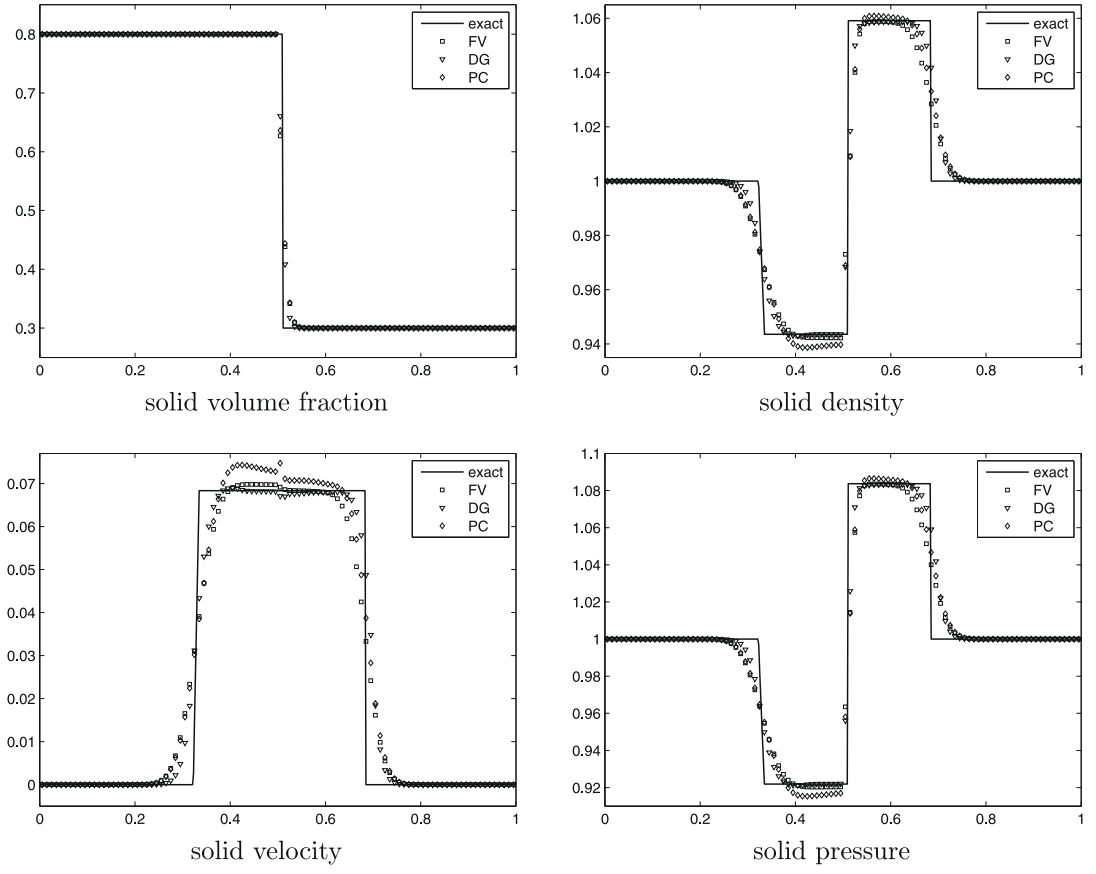

Fig. 4(b). Test 1. Results for the solid phase: computed (symbol) and exact solution (line) at time $t = 0.15$.

In principle, a wide variety of state Riemann solvers can now be applied. Examples include: the exact Riemann solver, linearized Riemann solvers, two-rarefaction Riemann solvers, two-shock type Riemann solvers and others. No practical experience on this approach has been reported in the literature. Using the canonical path (50) we have

$$\mathbf{D}^-_{j+\frac{1}{2}} = \widetilde{\mathbf{A}}^-_{j+\frac{1}{2}}\left(\mathbf{Q}_{j+\frac{1}{2}}(0) - \mathbf{Q}^n_j\right), \mathbf{D}^+_{j+\frac{1}{2}} = \widetilde{\mathbf{A}}^+_{j+\frac{1}{2}}\left(\mathbf{Q}^n_{j+1} - \mathbf{Q}_{j+\frac{1}{2}}(0)\right), \tag{56}$$

where $\widetilde{\mathbf{A}}^-_{j+\frac{1}{2}}$ and $\widetilde{\mathbf{A}}^+_{j+\frac{1}{2}}$ are obtained from numerical approximations to the following integrals

$$\widetilde{\mathbf{A}}^-_{j+\frac{1}{2}} = \int_0^1 \mathbf{A}\left(\varphi\left(s, \mathbf{Q}^n_j, \mathbf{Q}_{j+\frac{1}{2}}(0)\right)\right) ds, \quad \widetilde{\mathbf{A}}^+_{j+\frac{1}{2}} = \int_0^1 \mathbf{A}\left(\varphi\left(s, \mathbf{Q}_{j+\frac{1}{2}}(0), \mathbf{Q}^n_{j+1}\right)\right). \tag{57}$$

We use the five-point Gauss quadrature rule to calculate these integrals. Note that for the Baer–Nunziato equations the matrix **A** has a lot of zero elements, for which numerical integration is not needed. This fact allows to save computational time.

7. Assessment of HLLC-based numerical schemes

Here we test the performance of the HLLC Riemann solver implemented in three numerical methods, namely finite volume method, discontinuous Galerkin (DG) finite element method and a new variant of path conservative methods. The finite volume and path-conservative schemes are first-order accurate and the DG finite element method is second-order accurate in both space and time. The purpose of this section is to illustrate the wide range of applications of the approximate Riemann solver of this paper.

7.1. Riemann problems

We consider six test problems. The initial data consists of two constant states separated by a discontinuity at $x = x_0$, all the parameters are listed in Tables 14–16. Transmissive boundary conditions are imposed at $x = 0$ and $x = 1$. Figs. 4–9 show the computational results for all these tests. All the results presented below were computed using the mesh of $N = 100$ cells

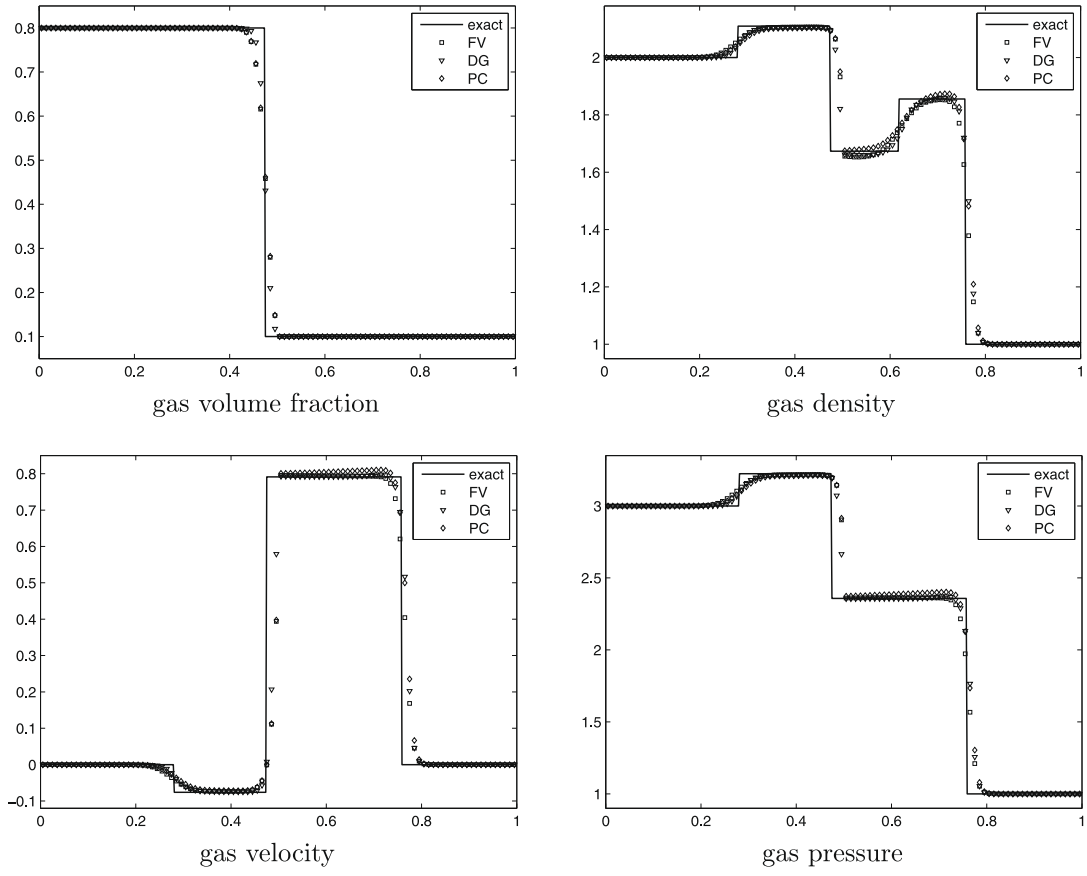

Fig. 5(a). Test 2. Results for the gas phase: computed (symbol) and exact solution (line) at time $t = 0.15$.

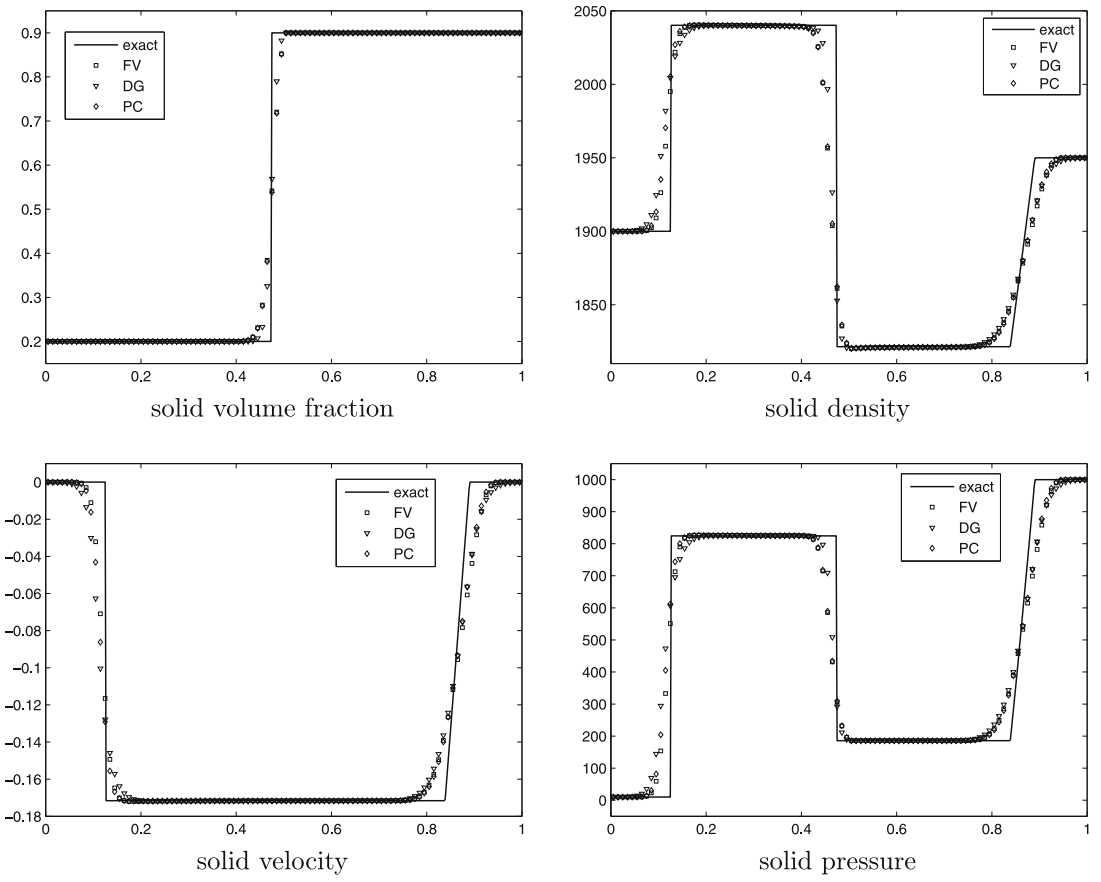

Fig. 5(b). Test 2. Results for the solid phase: computed (symbol) and exact solution (line) at time $t = 0.15$.

in the one-dimensional domain [0,1] at Courant number coefficient $C_{\mathrm{CFL}} = 0.9$, except for the RKDG method, for which the Courant number was taken equal to 0.6. We use the following estimation for the time step:

$$\Delta t^n = C_{\mathrm{CFL}} \Delta x / S^n_{\max},$$

where C_{CFL} is prescribed and the expression for $S^n_{\max}$ is given by

$$S^n_{\max} = \max_i \{|u^n_i| + a^n_i\}, \quad i = 1 \ldots N.$$

In each figure we present the results from three methods: finite volume (denoted as FV), Runge–Kutta discontinuous Galerkin (DG) and path-conservative (PC). The only test for which just finite volume and DG results are presented is the low-density case (Test 4), as the path-conservative scheme failed to compute a solution to this problem. For the other test cases we observe good agreement with the exact solution for all the three approaches.

7.1.1. Results for test 1

Test 1 was presented in [9] and results are shown in Figs. 4(a) and 4(b). The solid-phase wave pattern consists of a left rarefaction, a right shock wave and a right travelling solid contact, while the gas phase consists of a left rarefaction, a contact and a right shock wave. The equations of state for both phases are assumed ideal, with $\bar{\gamma} = \gamma = 1.4$. This is a rather mild test case, for which all of the three methods considered produce almost identical results, with path-conservative scheme producing larger errors in the solid phase velocity, density and pressure, see Fig. 4(b).

7.1.2. Results for test 2

Test 2 was also presented in [9] and results are shown in Figs. 5(a) and 5(b). This test problem is more demanding than Test 1 as it includes large variations of initial data and non-ideal EOS. For this problem the three methods are almost identical again.

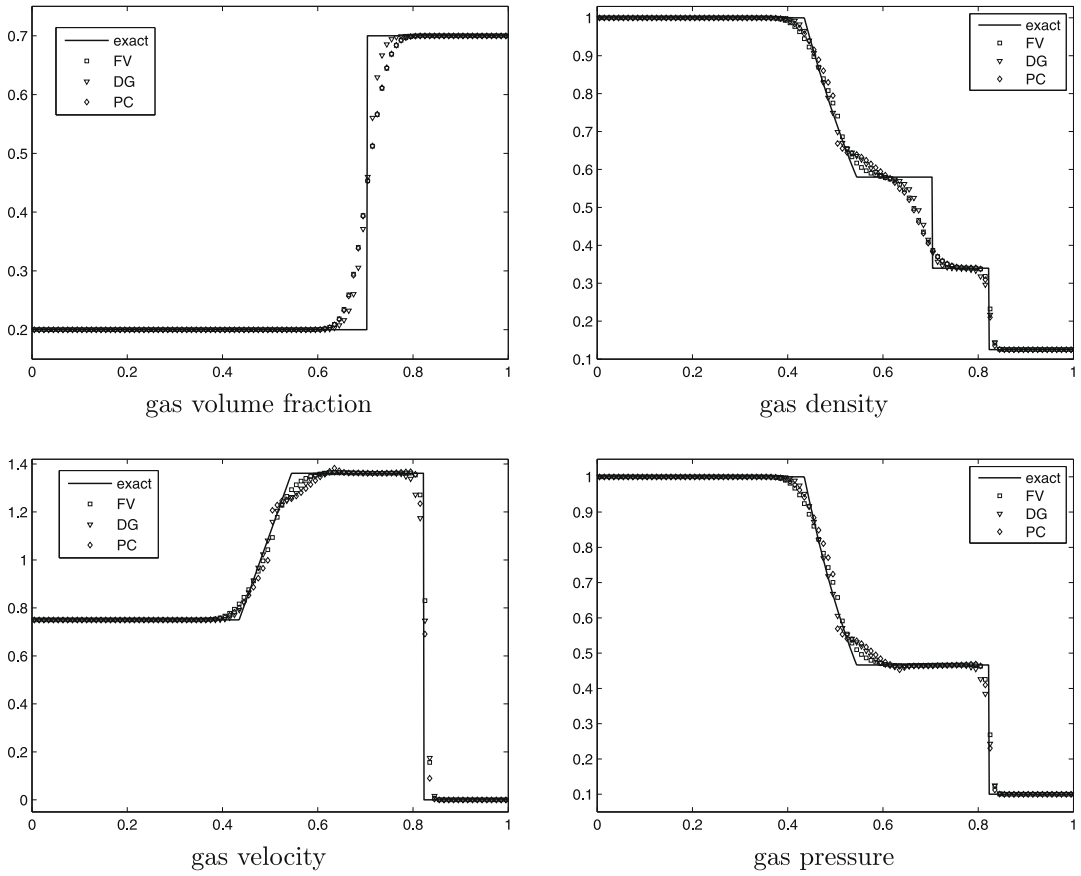

Fig. 6(a). Test 3. Results for the gas phase: computed (symbol) and exact solution (line) at time $t = 0.15$.

7.1.3. Results for test 3

Test 3 is an extended version of a test in [18] and results are shown in Figs. 6(a) and 6(b). The solution, for both phases, consists of a right shock wave, a right travelling contact discontinuity and a left sonic rarefaction wave. The correct resolution of the sonic point is very important in assessing the entropy satisfaction property of the numerical scheme. Among the schemes considered only the path-conservative approach generates a non-physical entropy glitch at the sonic point, which vanishes slowly with mesh refinement. The finite volume and discontinuous Galerkin methods do not experience any difficulties in resolving the sonic rarefaction wave.

7.1.4. Results for test 4

Test 4 is an extension of the so-called 123-problem [18] for two-phase flows and results are shown in Figs. 7(a) and 7(b). Both solid and gas phases consist of a two symmetric rarefaction waves and a trivial stationary contact wave. The region between the rarefaction waves is close to vacuum, therefore this test case is useful to assess the pressure positivity in different numerical methods.

The results of computations show that the finite-volume scheme with HLLC-type Riemann solver produces the most accurate solution, while the discontinuous Galerkin approach gives spurious oscillations that result in a severe slope limiting and very inaccurate resolution of phase volume fractions, which fortunately improves as the mesh is refined. The path-conservative method fails to compute the solution to this test problem. Note that the exact resolution of the volume fraction by the finite volume method is due to the present *complete* Riemann solver.

7.1.5. Results for test 5

Test 5 was designed to assess the ability of numerical methods to resolve the stationary isolated contact waves [18], the results are shown in Figs. 8(a) and 8(b). The exact solution allows the existence of the stationary contact waves in the solid and gaseous phases when the volume fraction and solid pressure gradients are present across the solid contact. The solution of this test problem contains isolated contacts in both solid and gas phases. As it can be seen from Figs. 8(a), 8(b), 8(c), 8(d) this type of discontinuities is resolved exactly by all three schemes considered, provided that the Riemann solver used is the HLLC-type two-phase solver of this paper.

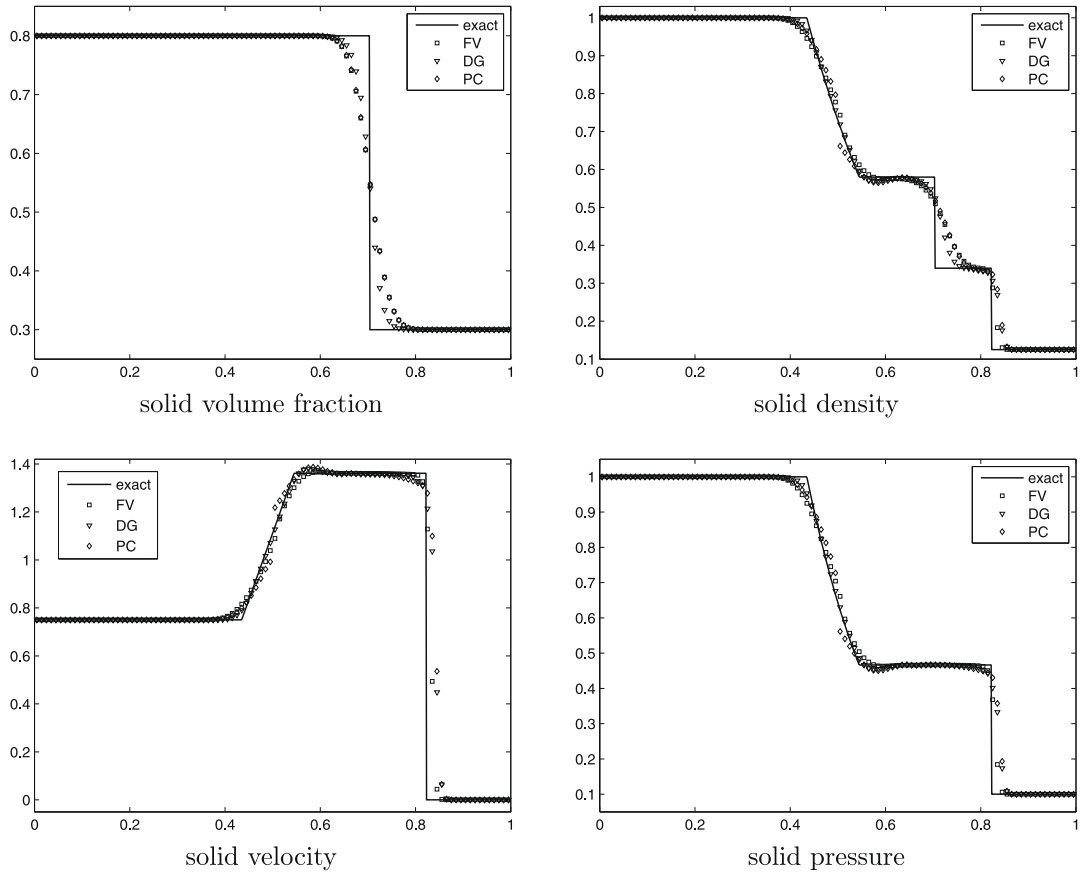

Fig. 6(b). Test 3. Results for the solid phase: computed (symbol) and exact solution (line) at time $t = 0.15$.

To compare the performance of the proposed HLLC-type Riemann solver with other solvers we present the results computed using the HLL-type flux suggested in [24] (see Figs. 8(c) and 8(d)). The solution was obtained by the finite-volume scheme under the same conditions on the mesh and the CFL number.

7.1.6. Results for test 6

Test 6 is the extension of a strong-shock test problem from [18], which was designed to assess the robustness and accuracy of numerical methods. The results are presented in Figs. 9(a) and 9(b). The solution of this problem contains, for each phase, a right travelling shock wave, a contact discontinuity and a left rarefaction wave. As the jump of initial pressures is very large, strong shock waves are generated in each phase; the distance between the right shock and contact waves is small in the gas phase. These flow features can lead to inaccuracies in numerical solution. For this test case the Riemann solver is more sensitive to the guess values in the Newton iteration. Comparing the results obtained by three numerical methods we observed that the most accurate solution was computed using discontinuous Galerkin methods, which is second order in space and time. Among the first-order schemes the finite-volume method proved to be more accurate.

7.2. Interaction of nearly pure fluids

In this section we study the performance of the proposed HLLC-type Riemann solver for the simulation of pure materials interaction in the framework of the finite volume method. Various examples of such test problems were introduced in [2,3].

We use the following initial data in our computations: the initial discontinuity is positioned at $x = 0.5$ in the computational domain $[0,1]$, values for left and right initial data are listed in Tables 17–19.

This test problem corresponds to the interaction of the nearly pure solid phase (on the left) and nearly pure gas phase (on the right), separated by the initial discontinuity. In order to simulate nearly pure materials the corresponding volume fraction is taken close to 1, namely, $\tilde{\alpha}_L = 1 - \varepsilon$ and $\alpha_R = 1 - \varepsilon$, where $\varepsilon = 10^{-6}$. The resulting exact solution to this problem repeats the solution of the Riemann problem for the Euler equations with the left and right initial data

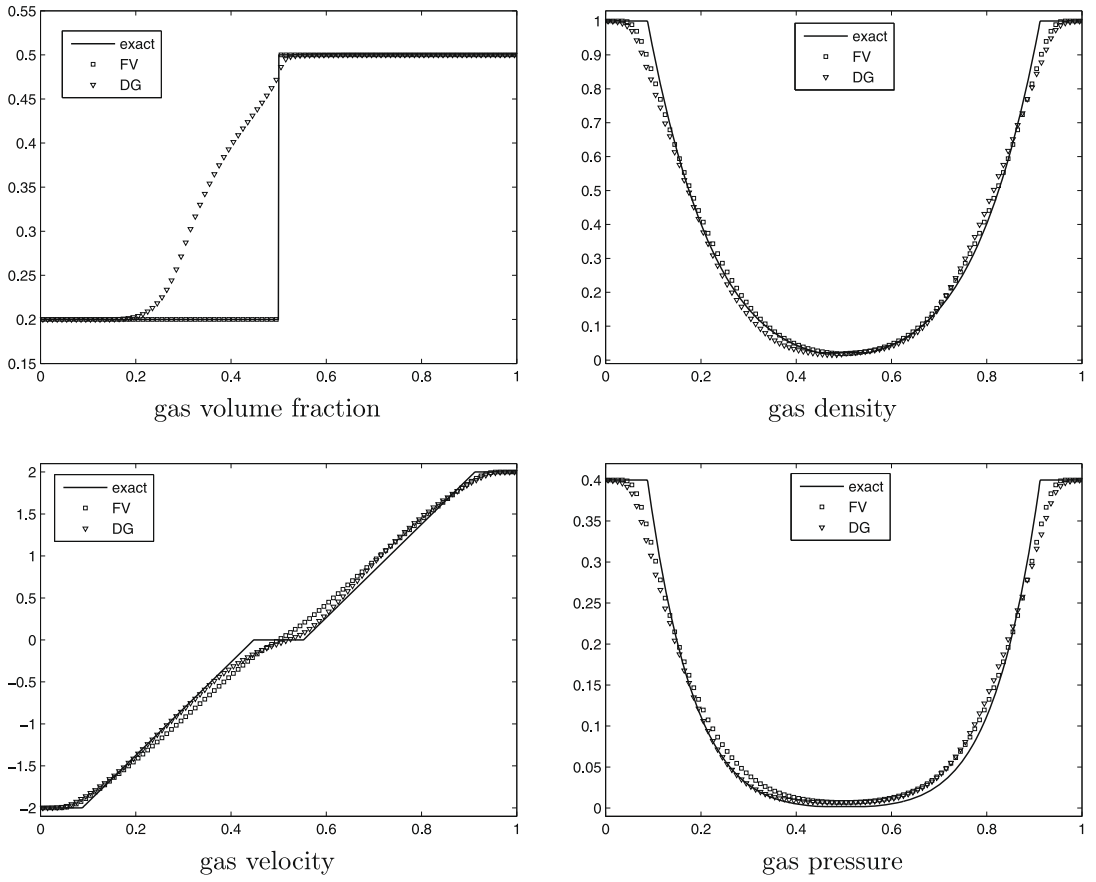

Fig. 7(a). Test 4. Results for the gas phase: computed (symbol) and exact solution (line) at time $t = 0.15$.

taken from the pure phase present on each side of the discontinuity; this property allows to choose arbitrary initial data for the material in the region where it almost vanishes, i.e. on that side of the initial discontinuity where the volume fraction equals to ε.

Fig. 10 shows the solution obtained with the proposed HLLC-type numerical flux incorporated in the finite volume scheme. We present the results computed at the CFL number 0.9 on three meshes of 100, 1000 and 5000 cells to illustrate the convergence of the method. The dashed vertical line separates the regions occupied by each of the fluids, namely, the solid phase is situated on the left of this line and the gas phase on its right.

It should be noted that certain difficulties were experienced in the numerical solution of the pure fluids interaction problems. Although the Riemann solver itself provides accurate solution to the problem locally, the overall numerical solution can not be computed by some of the methods. Thus, the considered discontinuous Galerkin and path-conservative schemes fail to compute the solution to the presented test problem involving very low volume fractions and high changes of pressures or densities on the interface, regardless of the numerical flux used. On the other hand, the finite volume method combined with the HLLC-type Riemann solver or the exact Riemann solver gives a good solution quality, as observed in Fig. 10. Finally, it is also worth mentioning that difficulties in the numerical solution of the interaction problems may occur if the initial data contains pressure jumps with the ratio more than 10^3, as it appears to be restrictive for the approximate Riemann solvers as well as for the exact Riemann solver.

Comparison of the results obtained by our numerical flux with the results computed with the exact flux [9] shows that the quality of the solution is virtually invariant, while our approximate numerical flux allows to reduce the computational time by 50–60%, which is advantageous for practical applications. The speed of the derived HLLC-type Riemann solver for the Baer–Nunziato equations was estimated and compared to the speed of the exact solver, measured on the same computational platform. Table 19 presents the average computational time (in seconds) for both solvers and their ratio.

The ratio of computational times for the implementation of the exact and approximate Riemann solvers is about 2.6, which means that the algorithm using the latter solver can be accelerated by 62% in average. The same ratio holds true for the whole algorithm including all the calculations, which means that the savings related purely to the flux are much more significant.

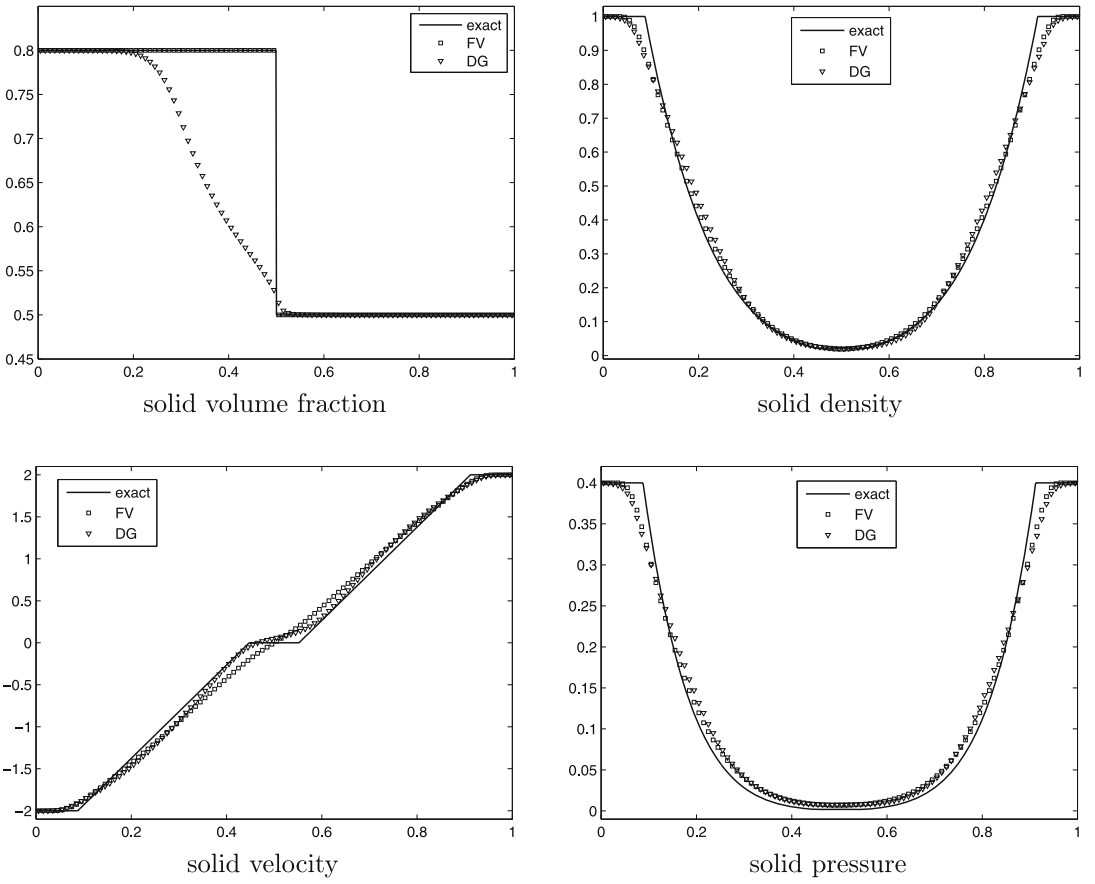

Fig. 7(b). Test 4. Results for the solid phase: computed (symbol) and exact solution (line) at time $t = 0.15$.

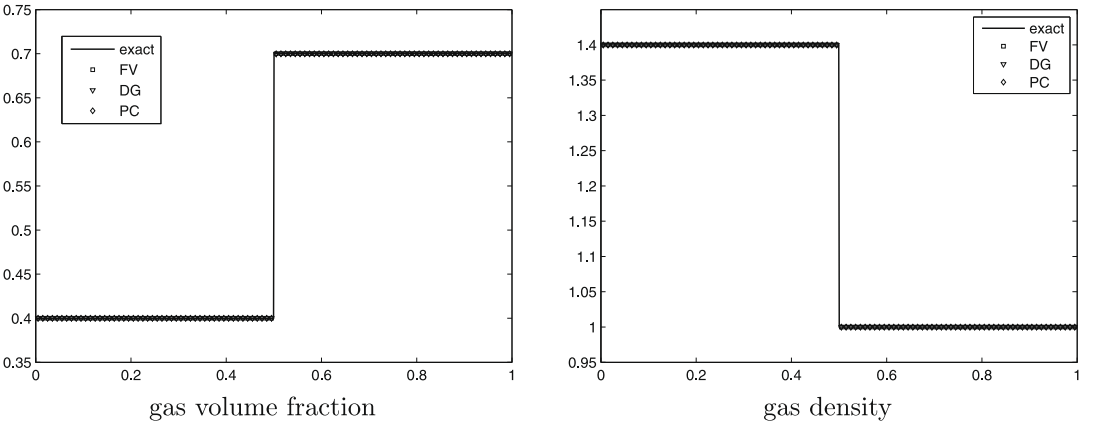

Fig. 8(a). Test 5. Results for the gas phase: computed (symbol) and exact solution (line) at time $t = 0.15$. HLLC-type Riemann solver.

8. Concluding remarks

We have solved approximately the Riemann problem for the split three-dimensional Baer–Nunziato equations of compressible two-phase flow for ideal and stiffened gas equations of state. The Riemann solver is nonlinear and complete, as it contains all the characteristic fields present in the exact solution of the Riemann problem. In particular the approximate Riemann solver is capable of recognizing exactly isolated linearly degenerate fields, such as contacts and shear waves. Solvers that do not possess this feature introduce excessive numerical dissipation in the overall solution.

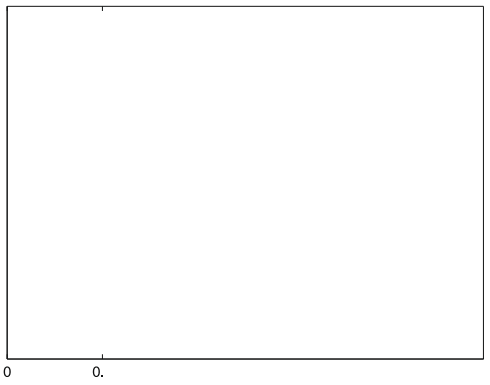

We have systematically assessed the solver by comparing the approximate solution with the exact solution for a series of carefully selected Riemann problems and found the approximate solution to be accurate for most cases considered.

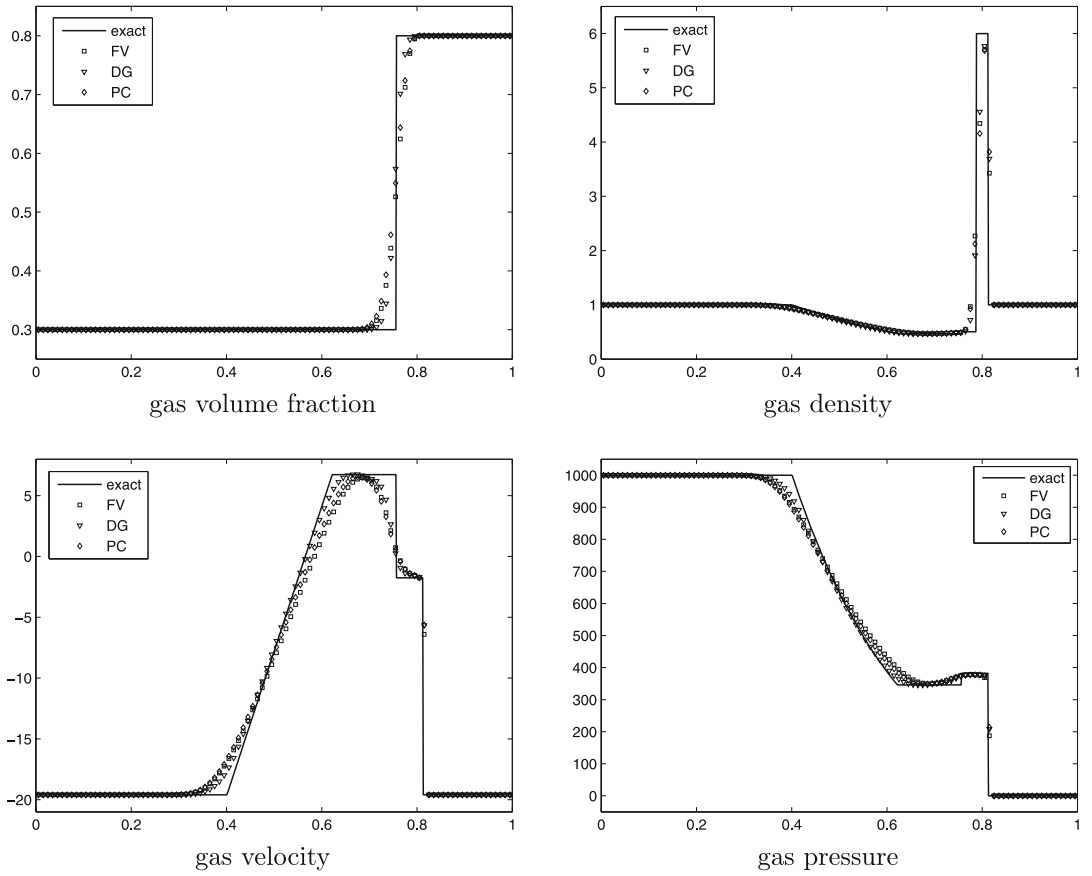

Fig. 9(a). Test 6. Results for the gas phase: computed (symbol) and exact solution (line) at time $t = 0.007$.

But the main use of the proposed Riemann solver is in the calculation of numerical fluxes for numerical methods intended for solving the general initial-boundary value problem. Thus we have implemented the approximate solver in the framework of finite volume, discontinuous Galerkin finite elements and path-conservative schemes. We have then thoroughly tested all the schemes on a series of demanding problems and found the schemes to be generally accurate and robust. The low-density test problem causes difficulties to the DG and the path-conservative scheme; the first one gave very inaccurate results for the stationary contact wave and the second one failed altogether. But we note that this is also the case for single-phase gas dynamics and not an exclusive feature of the Baer–Nunziato equations. We also compared the performance of the exact solver and our approximate solver as building blocks of the three numerical approaches described earlier. The obtained numerical results are virtually indistinguishable from each other but our approximate solver is significantly faster. Moreover, the approximate solver is also more robust than the exact solver. In a typical calculation one must solve thousand if not millions of local Riemann problems and the chances of finding a local Riemann problem for which the exact Riemann solver fails to converge are high. This fact renders the exact solver useless as a computational option.

The approximate Riemann solver of this paper can be used in a straightforward manner to solve the two- and three-dimensional Baer–Nunziato equations numerically, as the solution of the Riemann problem was given for the x-split three-dimensional equations, where x is the direction normal to an element interface in a computational setup. The solver could also be extended to deal with more complicated equations of state in order to solve realistic problems. Another possible extension is the treatment of purely *supersonic flow*, namely the flow satisfying the condition $(u - \bar{u})^2 > a^2$. For some applications one may also find locally supersonic flow, for which the solver must identify the situation automatically and respond appropriately. These issues are the subject of current investigations by the authors.

Acknowledgment

The first author acknowledges the financial support of the Italian Ministry of Research and Education (MIUR) in the framework of the research project PRIN2007, that in part made possible the work of this article.

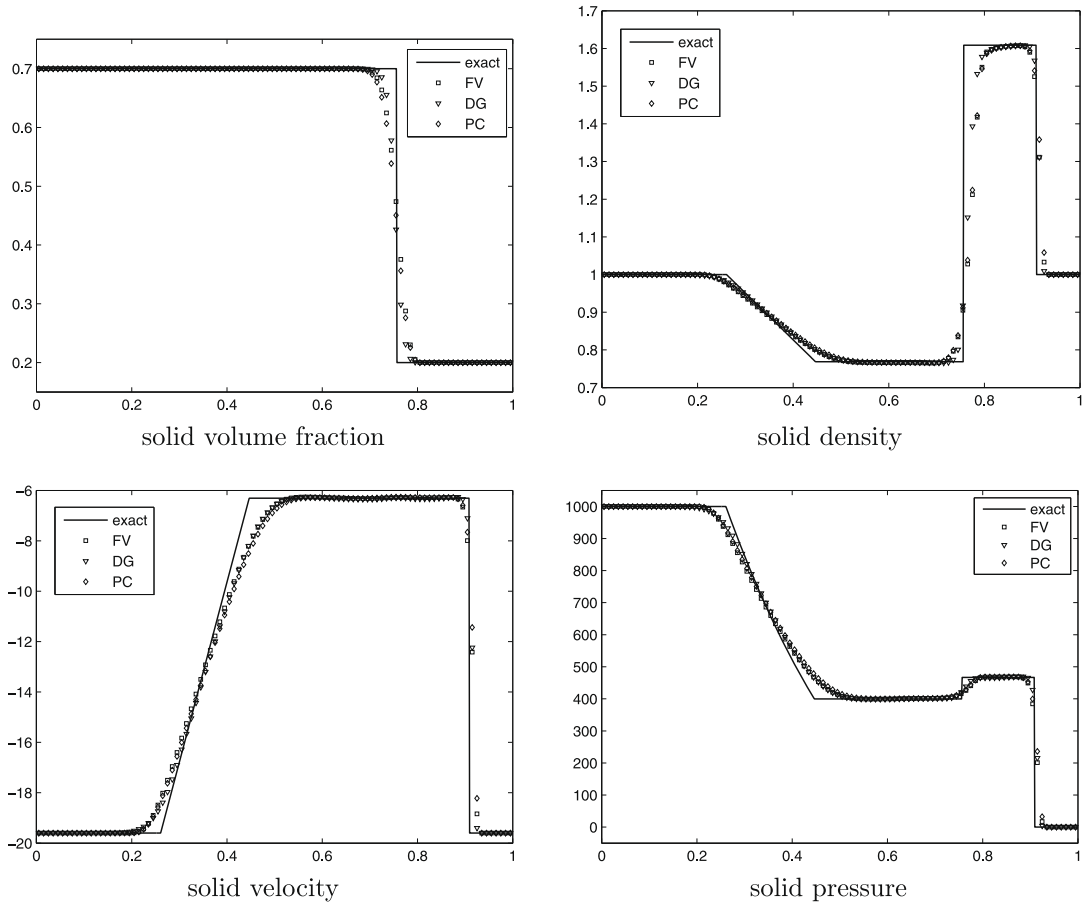

Fig. 9(b). Test 6. Results for the solid phase: computed (symbol) and exact solution (line) at time $t = 0.007$.

Table 17
Initial data (solid phase).

$\bar{\alpha}_L$	$\bar{\rho}_L$	$\bar{u}_L$	$\bar{p}_L$	$\bar{\alpha}_R$	$\bar{\rho}_R$	$\bar{u}_R$	$\bar{p}_R$
$1-\varepsilon$	10^3	0.0	2×10^7	ε	10^3	0.0	2×10^7

Table 18
Initial data (gas phase).

α_L	ρ_L	u_L	p_L	α_R	ρ_R	u_R	p_R
ε	50.0	0.0	10^5	$1-\varepsilon$	50.0	0.0	10^5

Table 19
Computational time.

	Time, 10^{-6} s
Exact RS	10.14
Approximate RS	3.9
Ratio	2.6

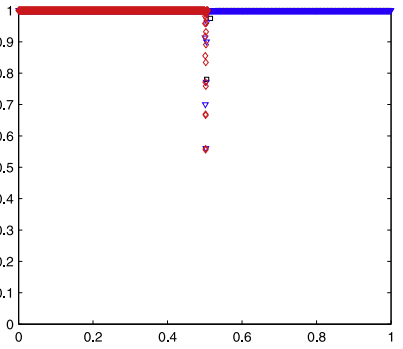
1
0.9
0.8
0.7
0.6
0.5
0.4
0.3
0.2
0.1
0
0
0.2
0.4
0.6
0.8
1

References

[1] M.R. Baer, J.W. Nunziato, A two-phase mixture theory for the deflagration-to-detonation transition (DDT) in reactive granular materials, J. Multiphase Flow 12 (1986) 861–889.
[2] R. Saurel, R. Abgrall, A multiphase godunov method for compressible multifluid and multiphase flows, J. Comput. Phys. 150 (1999) 425–467.
[3] R. Saurel, R. Abgrall, Discrete equations for physical and numerical compressible multiphase mixtures, J. Comput. Phys. 186 (2003) 361–396.
[4] B. Stewart, B. Wendroff, Two-phase flow: models and method, J. Comput. Phys. 56 (1984) 363–409.
[5] E. Romenski, E.D. Resnyanski, E.F. Toro, Conservative hyperbolic formulation for compressible two-phase flow with different phase pressures and temperatures, Quart. Appl. Math. 65 (2007) 259–279.
[6] V. Deledicque, M.V. Papalexandris, An exact Riemann solver for compressible two-phase flow models containing non-conservative products, J. Comput. Phys. 222 (2007) 217–245.
[7] P. Embid, M. Baer, Mathematical analysis of a two-phase continuum mixture theory, Cont. Mech. Thermodyn. 4 (1992) 279–312.
[8] N. Andrianov, G. Warnecke, The Riemann problem for the Baer–Nunziato model of two-phase flows, J. Comput. Phys. 195 (2004) 434–464.
[9] D.W. Schwendeman, C.W. Wahle, A.K. Kapila, The Riemann problem and a high-resolution Godunov method for a model of compressible two-phase flow, J. Comput. Phys. 212 (2006) 490–526.
[10] C. Parés, Numerical methods for nonconservative hyperbolic systems: a theoretical framework, SIAM J. Numer. Anal. 44 (2006) 300–321.
[11] E.F. Toro, Riemann-problem based techniques for computing reactive two-phase flows, Lecture Notes Phys. 351 (1989) 472–481.
[12] I. Toumi, An upwind numerical method for two-fluid two-phase flow models, Nucl. Sci. Eng. 123 (1996) 147–168.
[13] R. Saurel, R. Abgrall, A simple method for compressible multifluid flows, SIAM J. Sci. Comput. 21 (3) (1999) 1115–1145.
[14] H. Pailliere, A. Kumbaro, D. Bestion, S. Mimouni, A. Laporta, H. Staedtke, G. Franchello, U. Graf, P. Romstedt, E.F. Toro, E. Romenski, H. Deconinck, E. Valero, F. de Cachard, B. Smith, Advanced three-dimensional two-phase flow simulation tools for application to reactor safety (ASTAR), Nucl. Eng. Des. 235 (2005) 379–400.
[15] C.-H. Chang, M.-S. Liou, A robust and accurate approach to computing compressible multiphase flow: stratified flow model and AUSM+-up scheme, J. Comput. Phys. 225 (2007) 840–873.
[16] R. Saurel, O. Le Métayer, J. Massoni, S. Gavrilyuk, Shock jump relations for multiphase mixtures with stiff mechanical relaxation, Shock Waves 16 (2007) 209–232.
[17] M. Dumbser, A. Hidalgo, M. Castro, C. Parés, E. Toro, FORCE schemes on unstructured meshes ii: nonconservative hyperbolic systems, Comput. Methods Appl. Mech. Eng. 199 (2010) 625–647.
[18] E.F. Toro, Riemann solvers and numerical methods for fluid dynamics, Springer-Verlag, 2009.
[19] E.F. Toro, M. Spruce, W. Speares. Restoration of the contact surface in the HLL-Riemann solver. Technical Report CoA-9204, Department of Aerospace Science, College of Aeronautics, Cranfield Institute of Technology, UK, 1992.
[20] E.F. Toro, M. Spruce, W. Speares, Restoration of the contact surface in the HLL-Riemann solver, Shock Waves 4 (1994) 25–34.
[21] P. Batten, N. Clarke, C. Lambert, D. Causon, On the choice of wave speeds in the HLLC Riemann solver, SIAM J. Sci. Stat. Comput. 18 (1997) 1553–1570.
[22] P. Batten, M.A. Leschziner, U.C. Golberg, Average-state Jacobians and implicit methods for compressible viscous and turbulent flows, J. Comput. Phys. 137 (1997) 38–78.
[23] B. Cockburn, C.-W. Shu, Runge–Kutta discontinuous Galerkin methods for convection-dominated problems, J. Sci. Comput. 3 (2001) 173–261.
[24] S. Rhebergen, O. Bokhove, J.J.W. van der Vegt, Discontinuous Galerkin finite element methods for hyperbolic nonconservative partial differential equations, J. Comput. Phys. 227 (2008) 1887–1922.
[25] G. Dal Maso, P.G. LeFloch, F. Murat, Definition and weak stability of nonconservative products, J. Math. Pures Appl. 74 (1995) 483.
[26] A.I. Volpert, The space BV and quasilinear equations, Math. USSR Sbornik 73 (1967) 225–267.
[27] I. Toumi, A weak formulation of Roe's approximate Riemann solver, J. Comput. Phys. 102 (1992) 360–373.
[28] M. Luz Muñoz-Ruiz, C. Parés, Godunov method for nonconservative hyperbolic systems, Modélisation mathématique et analyse numérique 41 (2007) 169–185.